Synthesis of a novel, ternary AgI/CeO$_2$@g-C$_3$N$_4$ nanocomposite with exceptional stability and reusability for visible light-assisted photocatalytic reduction of hexavalent chromium

Mona Kohantorabi[1], Gholamreza Moussavi[1], Paula Oulego[2], Stefanos Giannakis[3]*

1. Department of Environmental Health Engineering, Faculty of Medical Sciences, Tarbiat Modares University, Tehran, Iran

2. Department of Chemical and Environmental Engineering, University of Oviedo, C/ Julián Clavería s/n., Oviedo, ES-33071, Spain

3. Universidad Politécnica de Madrid, E.T.S. Ingenieros de Caminos, Canales y Puertos, Departamento de Ingeniería Civil: Hidráulica, Energía y Medio Ambiente, Unidad docente Ingeniería Sanitaria, c/ Profesor Aranguren, s/n, ES-28040 Madrid, Spain

*Corresponding author Email: Prof. Dr. Gholamreza Moussavi, moussavi@modares.ac.ir

Abstract

This work demonstrates a highly efficient photocatalytic reduction of Cr(VI) to Cr(III) by using a AgI/CeO$_2$@g-C$_3$N$_4$ nanocomposite, under visible light (Vis) irradiation. The as-prepared samples were characterized by FT-IR, XRD, FE-SEM, TEM, XPS, DRS, PL, PC, and BET. Optimization of the treatment conditions included systematic parameterization, such as initial solution pH, photocatalyst dosage, and Cr(VI) concentration were investigated in the reaction. Compared with pure g-C$_3$N$_4$, CeO$_2$, AgI, and CeO$_2$@g-C$_3$N$_4$ binary nanocomposite, the as-made AgI/CeO$_2$@g-C$_3$N$_4$ ternary nanocomposite showed significantly higher photo-reduction efficiency. The ternary photocatalyst shows a 99.6% reduction efficiency for Cr(VI) (15 mg L^{-1}) within 75 min at pH=3.0. The highest rate constant value (0.058 min^{-1}) was calculated for ternary photocatalyst that is 2.1 times higher than CeO$_2$@g-C$_3$N$_4$/Vis process. The improved activity could be related to the effective electron/hole (e^-/h^+) pairs separation by forming a hetero-junction structure. The XPS analysis of recovered photocatalyst shows the presence only of Cr(III), which indicated a complete photo-reduction of Cr(VI) over AgI/CeO$_2$@g-C$_3$N$_4$ nanocomposite. Moreover, the as-made photocatalyst exhibited more than 91% reduction efficiency after four cycles under the optimum reaction conditions. Based on the radical trapping experiments, photo-generated electrons (e^-), and superoxide radicals ($O_2^{\bullet-}$) were the dominant active species in photo-catalytic Cr(VI) removal.

Keywords: *Cr(VI) photo-reduction, water treatment, photo-generated electron, visible light photocatalysis, advanced reduction process.*

Highlights

• A ternary AgI/CeO$_2$@g-C$_3$N$_4$ photocatalyst was fabricated for the first time.

• The photo-reduction of Cr(VI) was highly enhanced over AgI/CeO$_2$@g-C$_3$N$_4$.

• Acidic media was the most favorable in photocatalytic reduction of Cr(VI).

• Trapping experiments indicated that e$^-$, and O2·- were the dominant reactive species.

• The presence of AgI NPs can enhance the kinetics of photocatalytic reduction of Cr(VI).

Graphical Abstract
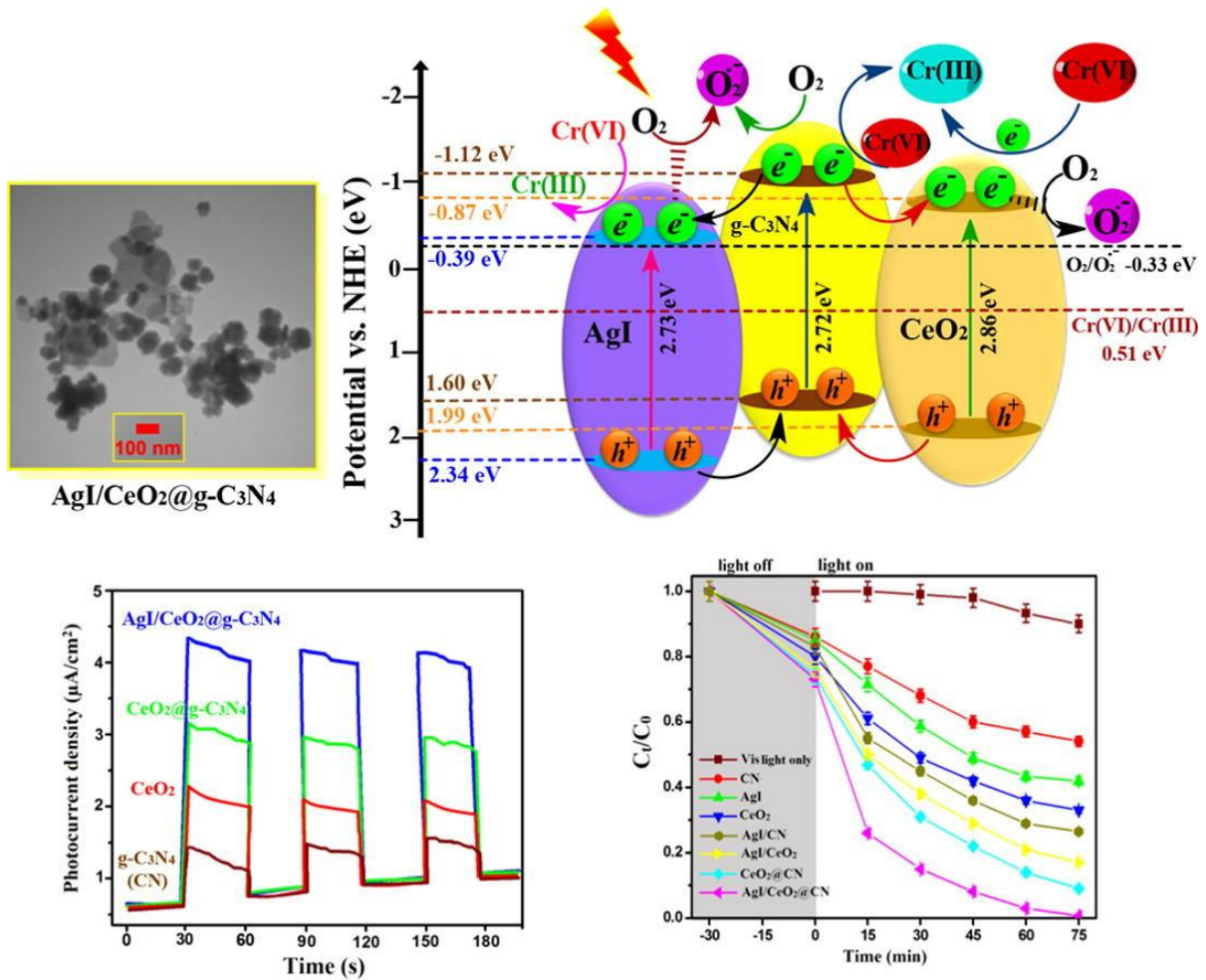
1. Introduction

Heavy metals are dangerous, anthropogenic toxic pollutants, and their excessive release into the environment has become a great concern [1]. Among these metals, hexavalent chromium (Cr(VI)), whose presence in industrial effluents derives from dye manufacturing, wood processing, leather, etc., can result in serious environmental and human health issues, due to its high solubility and toxicity [2,3]. According to World Health Organization (WHO) reports, the concentration of Cr(VI) in drinking water should not exceed 0.05 mg/L [4], and its high concentration (> 0.1 mg/L) can cause problems, such as cancer and fetal malformations in pregnant females [5].

Chromium exists in various oxidation states, such as Cr(VI) and Cr(III), among which Cr(III) has low toxicity, and can be easily transformed to $Cr(OH)_3$ in aquatic environments, while the hexavalent ion does not precipitate [6]. Consequently, many approaches have been developed for the removal of Cr(VI) from water such as adsorption [7], membrane filtration [8], electrochemical processes [9], ion exchange [10], and chemical precipitation [11]. All mentioned methods have problems in practical applications, due to the low removal efficiency of Cr(VI), high cost, and poor settleability of the precipitate during the reaction [12]. For these reasons, the development of efficient and friendly methods is important for the removal of Cr(VI) from industrial wastewaters. Compared to other technologies, photocatalysis is considered as a promising technique with high efficiency, and low energy consumption for transforming harmful compounds into harmless substances [13-15]. For instance, over the last decade, the photocatalytic reduction of Cr(VI) has been established as an effective -while green- process for the reduction of Cr(VI) to the harmless Cr(III) form, through suitable heterogeneous photocatalysts [16], such as TiO_2-based photocatalysts [17,18].

Graphitic carbon nitride (g-C_3N_4, hereon: CN) is a relatively recently-developed type of metal-free visible-light responsive photocatalyst, which has gained ground in photocatalytic applications, due its facile fabrication method, high stability, exceptional light adsorption, non-toxicity, thermal stability, and low-cost synthesis process [19, 20]. This semiconductor has a narrow band gap energy

($E_g = 2.7\ eV$), thanks to its sp^2 hybridization of carbon and nitrogen, and the formation of π-conjugated graphitic planes, which brings the capacity to harvest light [21]. However, due to its low specific surface area and the high recombination rate of electron-hole (e^-/h^+) pairs, the photocatalytic performance of CN is limited. Among the various modification processes of pure CN, coupling with other semiconductors is a promising way to enhance its photocatalytic performance by modifying its band gap, accelerating charge transfer, and increasing the number of active sites [22]. Great potential is found in cerium oxide (CeO$_2$), an important rare earth oxide that has been widely used in industrial applications such as catalysis, photocatalysis, solar and fuel cells [23, 24]. Despite its desirable features, its rapid e^-/h^+ recombination is its great limitation for widespread use in the photocatalysis field [25]. Therefore, the modification of CeO$_2$ with a material that will delay the electron recombination taking place, by enhancing the charge separation, could improve its photocatalytic activity [26].

Recently, plasmonic noble metal photocatalysts for water remediation were developed. Among these materials, silver halides (AgX, X = Cl, Br, and I) are considered as effective visible-light harvesting semiconductors [27]. For instance, AgI, with band gap energy around 2.7 eV [28], has been developed for photocatalytic applications due to its high performance under visible light. AgI was used for the modification of other semiconductors to enhance the light capacity, and improve the charge carriers transfer rate [28]. The main issue with AgI is its stability; it has been reported that during the reaction it can be converted to Ag^0 [29]. Hence, developing efficient methods for the fabrication of AgI-based photocatalysts have been considered [29].

Taking into account the aforementioned properties of materials, it is now understood why researchers have focused to the development of multi-component systems, especially CN-based nanocomposites such as AgCl/Ag$_3$PO$_4$/g-C$_3$N$_4$ [30], g-C$_3$N$_4$/Ag$_3$PO$_4$/AgI [31], AgI/LaFeO$_3$/g-C$_3$N$_4$ [32], and g-C$_3$N$_4$/CeO$_2$/ZnO [33], demonstrating high photocatalytic performance. In fact, fabrication of hetero-photocatalysts with matching band-gap energy is one of the most effective strategies for

improving the photocatalytic activity and promote the separation of charge carriers [34]. In addition, ternary photocatalysts show much higher photocatalytic efficiency compared to binary photocatalysts, due to their high electron transfer rate [35]. For example, Chen et al. fabricated a ternary $ZnTiO_3/Zn_2Ti_3O_8/ZnO$ photocatalyst, which showed high photocatalytic activity in degradation of organic pollutants and reduction of Cr(VI) [36]. They indicated that this efficient activity is related to the effective migration and separation of photo-generated charge carriers, and more active sites on the surface of ternary photocatalyst [36].

To the best of our knowledge, there is no report on the synthesis of CN-based ternary photocatalyst containing CN, CeO_2, and AgI NPs, that takes advantage the high responsiveness of CN, the properties of CeO_2 and the matching bandgap of AgI. Herein, a ternary $AgI/CeO_2@CN$ nanocomposite was fabricated by using facile (hydrothermal and precipitation) methods for this novel catalyst, and then used for the photocatalytic reduction of Cr(VI) to Cr(III). Moreover, the various operational parameters that affect Cr(VI) removal such as initial solution pH, catalyst concentration, and initial Cr(VI) concentration were systematically assessed. The stability and durability of novel nanocomposite was examined in consecutive photocatalytic cycles. Finally, in order to address the role of each reactive species produced during the reaction, radical trapping experiments were deployed, and a plausible mechanism for the elucidation of the enhanced, advanced reduction of Cr(VI) over a $AgI/CeO_2@CN$ nanocomposite was proposed.

2. Materials and Methods

2.1. Chemical and reagents

All solvents and reagents used in the present study were of analytical grade and used as received. Cerium nitrate hexahydrate ($Ce(NO_3)_3 \cdot 6H_2O$), ethylene glycol ($C_2H_6O_2$), acetic acid (CH_3COOH), methanol (CH_3OH), acetone (C_3H_6O), ethanol (C_2H_5OH), phosphoric acid (H_3PO_4), sodium hydroxide

(NaOH), and sulfuric acid (H_2SO_4) were purchased from Merck Co. The melamine powder ($C_3H_6N_6$) for the synthesis of graphitic carbon (g-C_3N_4), potassium dichromate ($K_2Cr_2O_7$), diphenylcarbazide (DFC, $C_{13}H_{14}N_4O$), silver nitrate ($AgNO_3$), potassium iodide (KI), and scavengers including *p*-benzoquinone (BQ), isopropyl alcohol (IPA), and potassium bromate ($KBrO_3$) were supplied from Sigma Aldrich. Distilled water (DI) was used for all synthesis processes and experiments.

2.2. Analytical techniques

The as-synthesized catalysts were characterized by an array of analytical methods. X-ray diffraction (XRD) measurements were used for the evaluation of the crystalline structure by using PW3050/60 X' Pert PRO diffractometer with a Cu Kα radiation (λ = 1.54060 A°). Fourier transport infrared (FT-IR) spectra was recorded on an ABB BOMER MB series spectrophotometer by using KBr pellets in the range of 500-4000 cm^{-1}. The surface morphology of the samples was investigated by field emission scanning electron microscopy (FE-SEM, Mira3 Tascan), and transmission electron microscopy (TEM, Philips-CM30 instrument). To study the oxidation states and binding energy of samples, X-ray photoelectron spectroscopy (XPS) was applied with a SPECS Phoibos 100 MCD5 hemispherical electron analyzer operating at a constant pass energy. Kα Mg (1253.6 eV) was the X-ray source employed together with a flood electron gun to compensate charge effects on the catalysts. The optical properties of the as-made nanocomposites were investigated by UV-Vis diffused reflectance spectroscopy (DRS, Shimadzu 2550-8030 spectrophotometer) in the wavelength range of 200-600 nm. The photoluminescence (PL) spectrum was recorded through FL3-TCSPC fluorescence spectrophotometer at ambient temperature. Brunauer-Emmett-Teller (BET) analysis for the evaluation of pore size distribution, and specific surface area was carried out on a Micromeritics/Gemini-2372 analyzer via N_2 adsorption/desorption at 77 K. The solution pH was adjusted by using a Jenway pH-meter (Jenway Co. UK). The photocatalytic Cr(VI) reduction reaction was monitored by using a UV-Vis spectrophotometer (Unico-UV 2100) at 540 nm according to the diphenylcarbazide (DFC) method [37].

2.3. Stepwise fabrication of the ternary AgI/CeO$_2$@g-C$_3$N$_4$ photocatalyst

2.3.1. Synthesis of CeO$_2$ nanospheres

CeO$_2$ nanospheres were prepared by a hydrothermal method [23]. Briefly, 2.3 mmol (1.0 g) of Ce(NO$_3$)$_3$·6H$_2$O was dissolved in 2.0 mL of DI water. Then, 1.0 mL of acetic acid was added dropwise into the above mixture, and mixed under ultrasound for 15 min. Subsequently, 30.0 mL of ethylene glycol (EG) was added, and the suspension was stirred at room temperature for 30 min. The obtained clear solution was transferred into a Teflon-lined stainless-steel autoclave, and heated at 180 °C for 200 min. After cooling to ambient temperature, the obtained white products were collected by centrifugation, and washed several times with water/ethanol, and then dried at 70 °C overnight.

2.3.1. Synthesis of the CeO$_2$@g-C$_3$N$_4$ (CeO$_2$@CN) nanocomposite

The graphitic carbon nitride was synthesized by using a previously reported method [24]. Briefly, a melamine was placed into an alumina crucible in the muffle furan, and heated at 550 °C for 2 h, following at 500 °C for 2 h with heating rate of 2.0 °C/min. The CeO$_2$@CN nanocomposite was prepared by a facile method. At first, 0.05 g of as-prepared CN was dispersed in to 30 mL of EG, and named as solution A. In the other vial 0.5 g of Ce(NO$_3$)$_3$.6H$_2$O was dissolved in 1.0 mL of DI water, and then 500 μL of acetic acid was added dropwise to the mixture (solution B). The solution A was added to solution B, and mixed under stirring for 30 min. Then, the suspension was transferred into the Teflon-lined stainless-steel autoclave, and heated at 180 °C for 200 min. Afterwards, the products were gathered by centrifugation, washed with mixture water/ethanol, and then dried at 65 °C for 8 h.

2.3.2. Preparation of AgI nanoparticles decorated on the CeO$_2$@CN nanocomposite

The AgI nanoparticles (NPs) were synthesized by using precipitation method. At first step, 0.2 g of as-made CeO$_2$@CN nanocomposite was dispersed in 25.0 mL of DI water under ultrasonic for 30

min. Then, 15.0 mL of an $AgNO_3$ solution (0.05 M) was dropwise added into the above mixture under stirring. The solution was mixed under continuous stirring for 1 h in the dark. Afterwards, 15.0 mL of KI solution (0.05 M) was added into the above mixture under stirring. By the addition of KI solution, a yellow color was observed into the mixture, which indicated the formation of AgI NPs on the surface of the CeO_2@CN nanocomposite. Moreover, pure AgI NPs were prepared by using the above method, in the absence of CeO_2@CN nanocomposite.

2.4. Photocatalytic experiments

In order to investigate the photocatalytic activity of the as-made samples, namely CeO_2, g-C_3N_4 (CN), AgI, CeO_2@CN, and AgI/CeO_2@CN nanocomposites, photocatalytic reduction of aqueous Cr(VI) to Cr(III) under visible light was selected. A Xenon lamp (35 W, 12 V) was used at the top of reactor with a filter cut off wavelength (only $\lambda > 420$ nm emitted), as the visible light source during the photocatalytic process. The reaction was carried out at room temperature, in a quartz reactor containing 50 mL of Cr(VI) solution (15.0 mg L^{-1}), and 10 mg of photocatalyst (as a starting point). Prior to the light irradiation, in order to evaluate the adsorption/desorption of as-made samples in this reaction, the reaction was carried out at dark for 30 min, and then the solution was irradiated with visible light. During the irradiation at certain intervals time (e.g., 0, 15, 30, 45, 60, and 75 min), 5.0 mL of reaction solution was taken, filtered using 0.22-μL PTFE membranes and then the Cr(VI) concentration was evaluated by the diphenylcarbazide (DFC) method [37]. Briefly, a stock solution of DFC was prepared by the dissolving of 0.25 g of DFC in 50.0 mL of acetone. Afterward, the obtained reaction solution (5.0 mL) was diluted with DI water (50 mL). The solution was transferred into the vial, three drops of concentrated phosphoric acid was added dropwise, and was shaken for five minutes. Subsequently, 10-12 drops of sulfuric acid (0.2 N) were added until the pH solution dropped to 2.0-2.5. Afterward, 1.0 mL of DFC solution was added into the mixture, and the vial was

mixed vigorously and kept standing for 10 min. Finally, the concentration of Cr(VI) was determined

spectrophotometrically at λ = 540 nm.

After the reaction, the catalyst was separated from the reaction media by high-speed centrifugation,

washed three times with water/ethanol, and finally dried at 70 °C. The recyclability and stability of

as-prepared photocatalyst was investigated in consecutive cycles of photo-reduction of Cr(VI) under

the same reaction conditions. All experiments in this study were performed at least in duplicate

series and two technical replicates.

3. Results and discussion

3.1. Characterization of the prepared photo-catalysts

To evaluate the chemical structure and the functional groups present in the as-made samples, the

FT-IR spectra was recorded by using the KBr pellet method (Fig. 1A). The pure CeO_2 [38], CN [39],

and AgI [40] showed identical characteristic to those reported in the literature. As it can be seen

from the results, the broad peak located at 3443 cm^{-1} is related to the O-H stretching vibrations of

water adsorbed on the surface of samples. In the FT-IR spectra of pure CeO_2 NPs, the absorption

peak at 550.8 cm^{-1} is related to the Ce-O band [38]. The mentioned peak was observed in the FT-IR

spectra of CeO_2@CN, and AgI/CeO_2@CN catalysts that indicated the presence of CeO_2 NPs in all the

catalysts. Also, the bands at 1623 cm^{-1} and 3376 cm^{-1} are related to the water and hydroxyl stretches,

respectively [38]. The additional band centered at 1384.3 cm^{-1} corresponds to the stretch band of

N-O, owing to the presence of nitrate [38]. In the FT-IR spectra of pure CN, CeO_2@CN, and

AgI/CeO_2@CN, the adsorption bands at 810 and 889 cm^{-1} are attributed to the typical breathing

mode of tri-s-triazine units and the deformation mode of N-H bonds, respectively [39] (Fig. 1a). In

addition, the broad adsorption bands from 3300 to 3000 cm^{-1} correspond to the stretching vibration

modes of N-H bonds [39]. The presence of absorption peaks centered at 1252 cm^{-1}, 1323 cm^{-1}, 1408

cm^{-1}, and 1568 cm^{-1} are attributed to the C-N stretching, while the absorption peak at 1635 cm^{-1} is

10

related to the stretching vibration mode of C-N [23]. Hence, all the peaks which correspond to CN and CeO_2 were detected in the FT-IR spectra of CeO_2@CN and AgI/CeO_2@CN nanocomposites, indicating the successful preparation of the intended photocatalysts.

The phase purity and the crystalline structure of the samples, including CeO_2, CN, AgI, CeO_2@CN, and AgI/CeO_2@CN nanocomposites, was studied by using X-ray diffraction (XRD) spectrometry (Fig. 1b). For the pure CN, the observed characteristic peaks at 13.0°, and 27.5° are assigned to the (001), and (002) planes of the graphite-like hexagonal phase of $g-C_3N_4$ (JCPDS No. 87-1526) [23]. As it can be seen from the obtained results, the diffraction peaks centered at 28.5°, 33.1°, 47.5°, 56.4°, 59.1°, 69.4°, and 76.7° are related to the (111), (200), (220), (311), (222), (400), and (331) planes of cubic phase of CeO_2 NPs (JCPDS No. 00-004-0593) [23]. Also, the main diffraction peaks of AgI NPs were observed at 21.3°, 23.7°, 39.2°, and 46.3° that are attributed to the (100), (002), (110), and (112) planes, respectively (JCPDS No. 09-0374) [41]. All the characteristic peaks of CN were observed in XRD patterns of CeO_2@CN nanocomposite, which confirmed the formation of the binary nanocomposite (CeO_2@CN) by the reported method. Moreover, in the XRD patterns of AgI/CeO_2@CN nanocomposite, two main peaks were detected which are related to the AgI and confirmed the presence of AgI NPs on the CeO_2@CN nanocomposite.
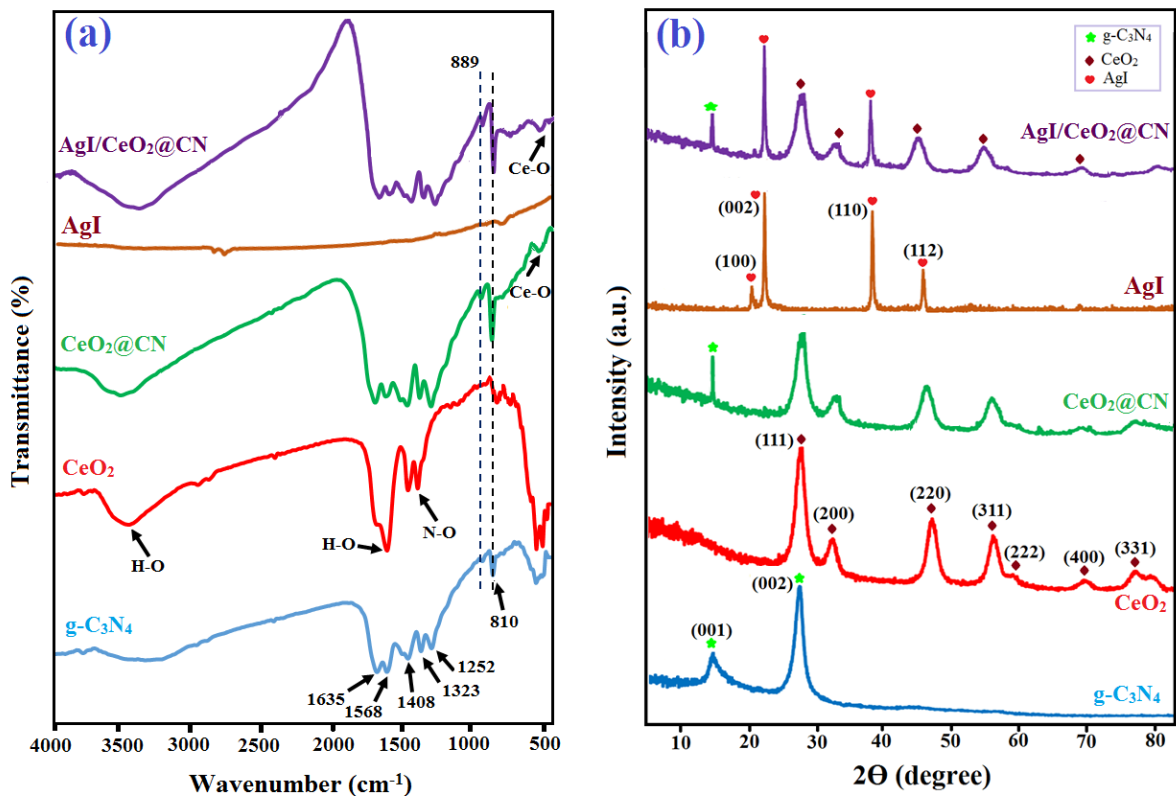
Figure 1. FT-IR spectra (a), and XRD patterns (b) of g-C₃N₄ (CN), CeO₂, CeO₂@CN, AgI, and AgI/CeO₂@CN nanocomposite.

Fig. 2 (a-c) illustrates the TEM images of CeO_2 NPs, and AgI/CeO_2@CN nanocomposite. As it can be seen from the TEM images, spherical CeO_2 NPs were obtained. Moreover, the CeO_2 nanospheres have an average particle size of 115.0 nm, as estimated form the histogram of the particle size (Fig. 2b). The presence of CN in the as-made AgI/CeO_2@CN nanocomposite is clearly observed form the TEM images of this catalyst (Fig. 2b, and c). The CeO_2 NPs with spherical structure were also observed from the FE-SEM images of the as-prepared nanocomposite (Fig 2. d, and e). In addition, the presence of AgI NPs were confirmed from these images. The elemental mapping was acquired to determine the composition of AgI/CN@CeO_2 nanocomposite (Fig. 2 f-m). The presence of elemental including carbon (C), nitrogen (N), cerium (Ce), oxygen (O), silver (Ag), and iodine (I) was confirmed

12

within the nanocomposite. In addition, all of these elements were distributed uniformly in the as-made nanocomposite.
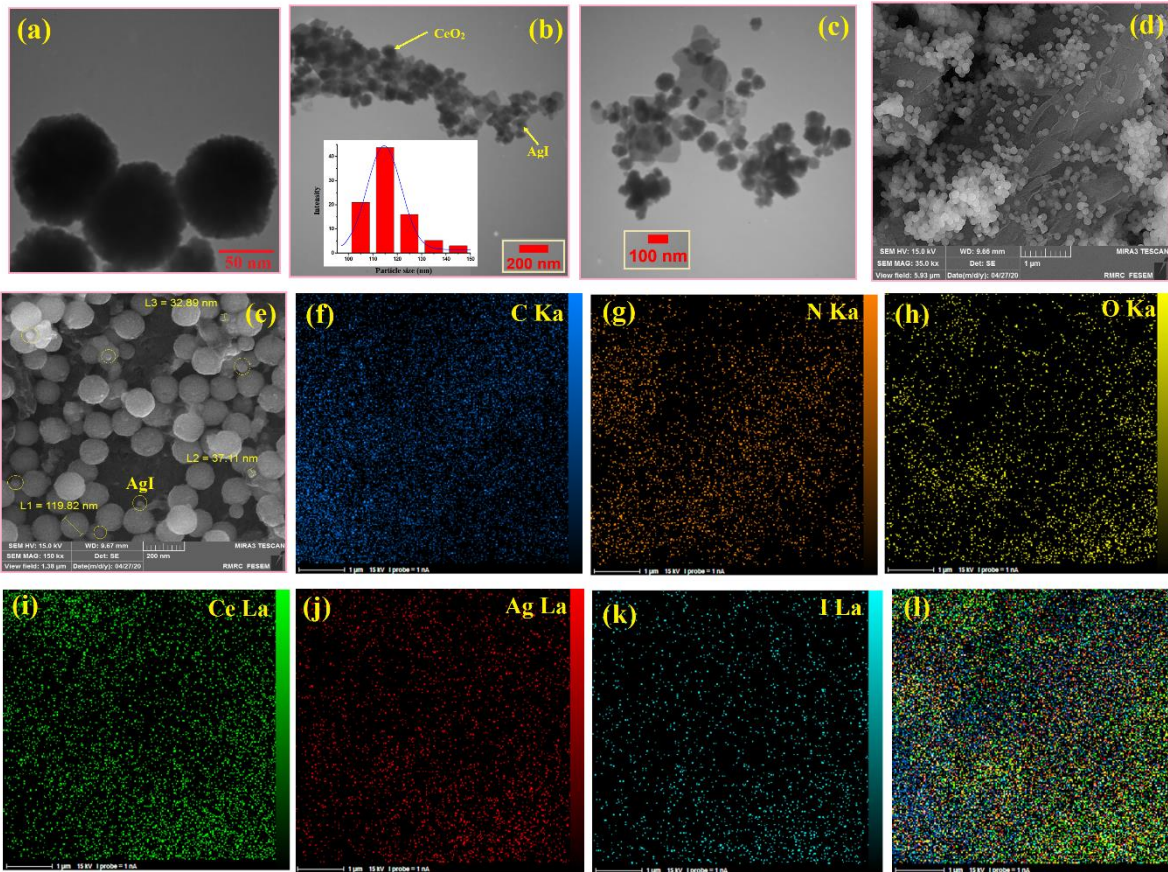
Figure 2. TEM images of CeO_2 NPs (a), and $AgI/CeO_2@CN$ nanocomposite (b, and c). FE-SEM images of $AgI/CeO_2@CN$ nanocomposite (d, and e). Elemental mapping of carbon (f), nitrogen (g), oxygen (h), cerium (i), silver (j), iodine (k), and $AgI/CeO_2@CN$ nanocomposite (l).

In order to investigate the surface chemistry and chemical states of the elements, XPS analysis was performed, and the obtained results were reported in Fig. 3. As it can be seen from the XPS survey scan of $AgI/CeO_2@CN$ nanocomposite, presence of elements including Ce, C, N, O, Ag, and I were confirmed by this analysis (Fig. 3a). Besides, the high resolution XPS spectra of O1s, Ce3d, C1s, N3f, Ag3d, and I3d are shown in Fig 3 (b-g). In the XPS spectra of C1s (Fig. 3b), two peaks at 284.6 eV, and 288.1 eV are attributed to the graphitic species (C-C), and C-N-C coordination in graphitic carbon nitride, respectively

[24, 42]. The XPS spectra of N1s is deconvoluted into the three peaks centered at 398.5 eV, 399.4 eV, and 400.6 eV, which are assigned to the sp^2 hybridized nitrogen in aromatic rings (C-N=C), nitrogen atoms bounded to the tertiary carbon (N-C$_3$), and amino group (-C-N-H), respectively [43]. In the high-resolution spectra of Ce3d, the bands labeled v_0, v_1, v_2, v_3 and u_0, u_1, u_2 represent satellite properties arising from the Ce3d$_{5/2}$, and Ce3d$_{3/2}$, respectively [44]. Moreover, the dominant peaks at v (880.2 eV), v_2 (888.2 eV), v_3 (896.3 eV) and u (898.3 eV), u_2 (914.5 eV) are characteristic for the Ce^{4+} species. The presence of Ce^{3+} species was confirmed by the observed peaks at positions labeled v_0, v_1 and u_0, u_1. Therefore, the Ce3d spectrum consists of the mixture of both Ce^{3+}, and Ce^{4+} ions. As observed in Fig. 3k, two peaks centered at 374.16 eV, and 368.13 eV in Ag3d spectrum are assigned to Ag3d$_{3/2}$, and Ag3d$_{5/2}$, respectively [45, 46]. These findings indicated that no metallic silver (Ag^0) appears in AgI/CeO$_2$@CN nanocomposite and indicated the successful preparation of AgI nanostructure during the synthesis process. Also, the two resolved peaks located at 630.7 eV and 619.1 eV are related to the I3d$_{3/2}$, and I3d$_{5/2}$, respectively that confirmed the presence of I element in the form of I$^-$ in as-made nanocomposite is (Fig. 3l) [45]. The XPS spectrum of O1s shows a peak centered at 529.8 eV that can be assigned to the Ce-O bond in CeO$_2$ structure [45]. Moreover, the peak at 532.4 eV in spectrum of O1s was attributed to the hydroxyl group.
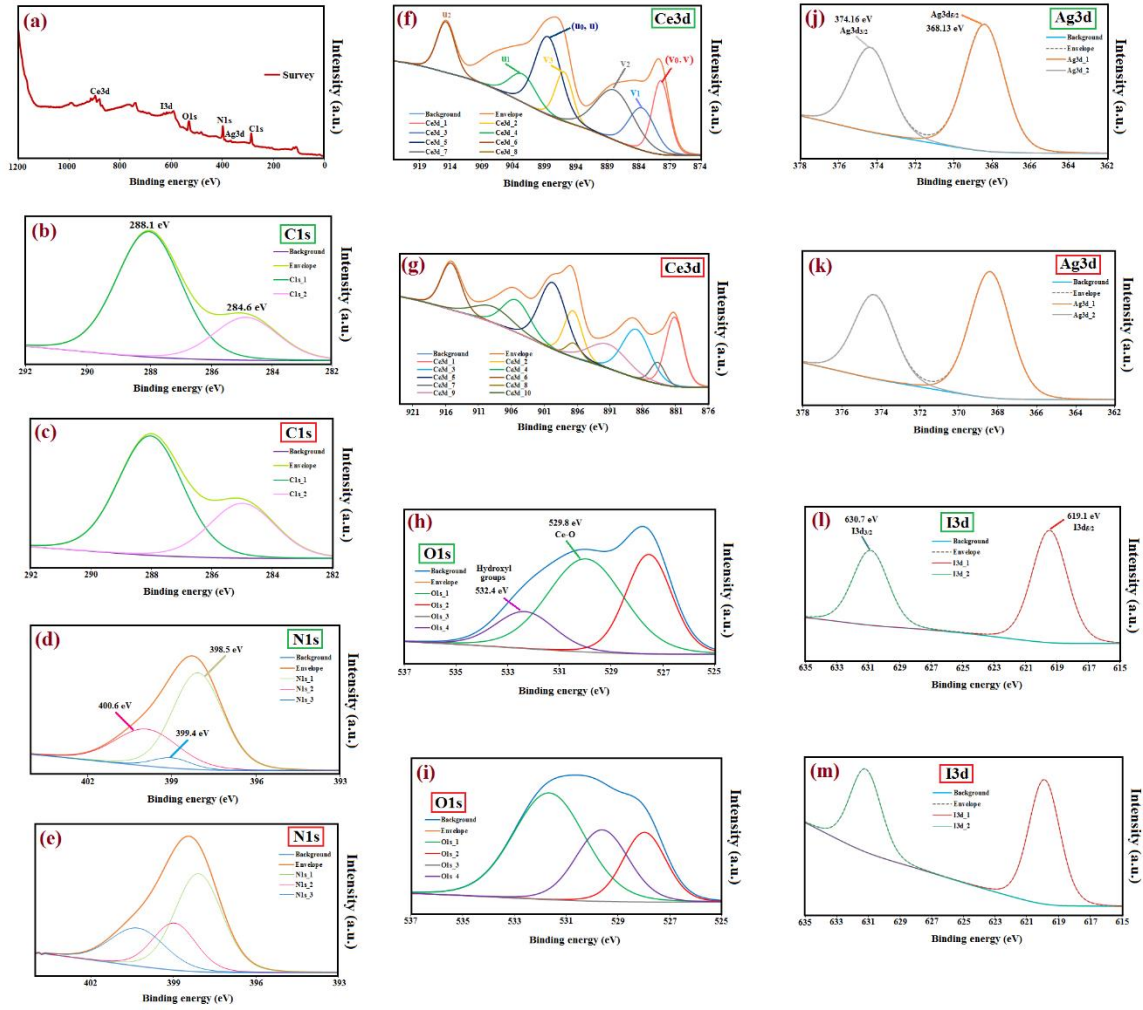
Figure 3. XPS survey spectra of AgI/CeO$_2$@CN nanocomposite (a), and high-resolution spectra of C1s (b, c), N1s (d, e), Ce3d (f, g), O1s (h, i), Ag3d (j, k), and I3d (l, m) of fresh and reused catalyst, respectively.

The optical properties and band gap energy of samples were studied by UV-Vis DRS analysis at room temperature, and the results are illustrated in Fig. 4a. The optical band gap energies (E_g) of samples were calculated by the Tauc/David-Matt model (eq. 1) as follows:

$$(Ah\nu) = \alpha\,(h\nu - E_g)^{n/2} \tag{1}$$

Where, *A*, *h*, *v*, and *a* are constant values; Plank's constant, high frequency, and absorption coefficient, respectively [47]. The band gap energies of samples were obtained by plotting ($ah\nu$)^2 versus E_g, as shown in Fig. 4b. The band gap energy values for CN, CeO$_2$ NPs, CeO$_2$@CN, and

15

AgI/CeO$_2$@CN were calculated to be 2.72 eV, 2.86 eV, 2.80 eV, and 2.63 eV, respectively. The edge potential values of conduction (CB), and valence bands (VB) of as-made photocatalysts were predicted by using following equations (eqns. 2, and 3):

$$E_{VB} = \chi - E^e + 0.5\, E_g \tag{2}$$

$$E_{CB} = E_{VB} - E_g \tag{3}$$

In which, χ, E^e, E_{VB}, and E_{CB} are corresponding to the absolute electronegativity, free energy of electron in the hydrogen scale (about 4.5 eV), energy level of VB, and energy level of CB, respectively [48]. Based on these equations and the bang gap energies calculated from eq. 1, the CB energy level of CN, CeO$_2$, and AgI were calculated to be -1.12 eV, -0.87 eV, and -0.39 eV, and these values for VB energy levels were obtained to be 1.60 eV, 1.99 eV, and 2.34 eV, respectively.

In order to address the separation efficiencies of the photo-generated charge carries in the as-made catalysts, their photoluminescence (PL) spectra were reported (Fig. 4c). According to the obtained results, pure CN and all the as-made nanocomposites show a broad peak in the range of 400-600 nm. Lower PL intensity signal indicates a lower recombination rate of photo-generated electron/holes (e^-/h^+) pairs in AgI/CeO$_2$@CN photocatalyst that leads to high photocatalytic performance, while high intensity of PL signal resulting the lower photocatalytic activity [49]. Based on the results, the presence of CeO$_2$ on the surface of CN significantly reduces the PL intensity, which can slow down the recombination of e^-/h^+ pairs. Also, as it can be seen from the results, the weakest PL peak was obtained for ternary nanocomposite that confirmed the favorable recombination rates of e^-/h^+ pairs in this sample.
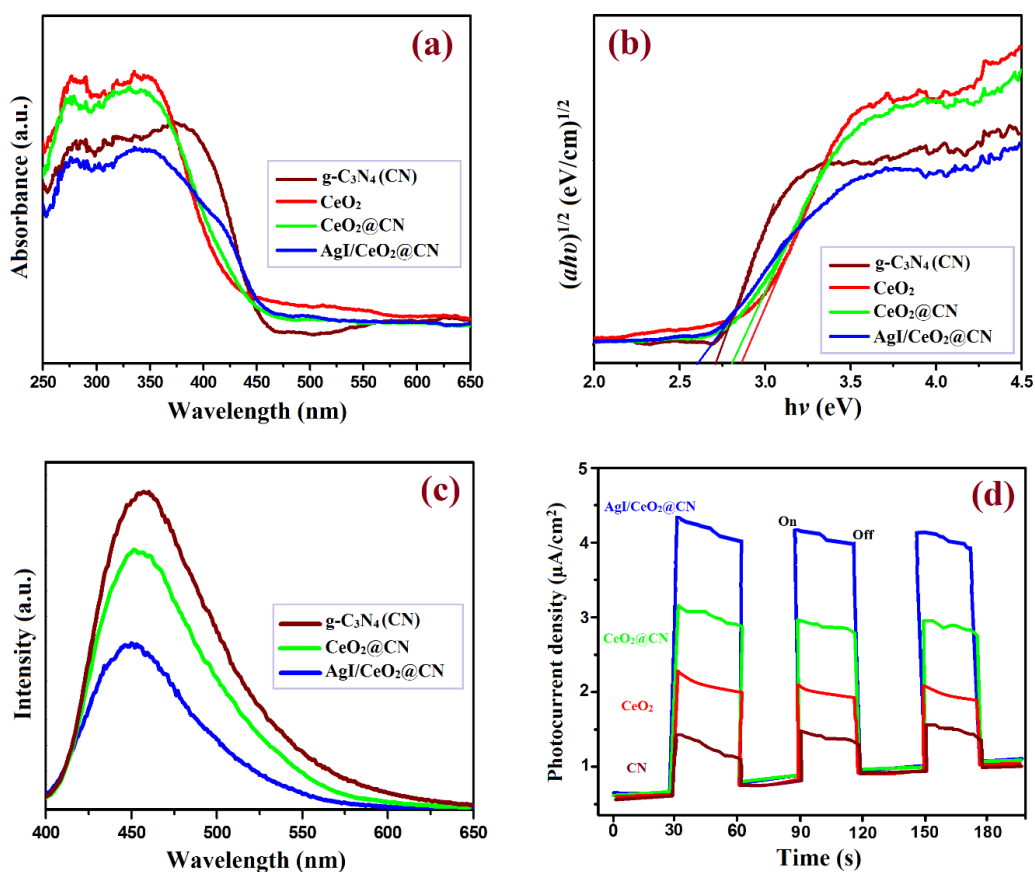
Figure 4. UV-Vis diffuse reflectance spectra (a), Tauc's plots (b), photoluminescence (PL) spectra (c), and transient photocurrent (PC) curves of as-prepared samples (d).

Fig. 4d displays the photocurrent (PC) response for the as-made samples during on and off cycles. The changes in currents confirm the charge transport of the samples. Compared to pure CN and CeO_2 NPs, our binary nanocomposite ($CeO_2@CN$) can promote the separation efficiency of the photo-generated e^-/h^+ pairs. The PC response decreases in the order of $AgI/CeO_2@CN$ > $CeO_2@CN$ > CeO_2 > CN. The PC intensity of the ternary photocatalyst was 1.4, 2.0, and 3.1 times higher than $CeO_2@CN$, CeO_2, and pure CN, respectively. This property increased the charge carriers transport, photocatalytic active sites, and reduced the recombination rate of e^-/h^+ pairs. Hence the ternary nanocomposite is expected to present the best photocatalytic performance.

In order to estimate the specific surface area of the as-prepared samples, N_2 adsorption-desorption isotherms were obtained and are depicted in Fig. 5. Also, the pore volume of structures was

17

determined via the Barret-Joyner-Halenda (BJH) method. According to the IUPAC classification, both of samples show the type IV isotherm with a H3-type hysteresis loop that indicate their mesoporous structure [20, 50]. The surface area of pure CN, and AgI/CN@CeO$_2$ nanocomposite was calculated to be 20.1 m^2 g^{-1}, and 110.3 m^2 g^{-1}, respectively. Compared to pure CN, the ternary photocatalyst showed the higher specific surface area that can be related to the formation of new pores [51]. In fact, the large surface area of the nanocomposite can provide more active sites for the adsorption of reactant compounds, and facilitate the photo-excited charge transfer [52]. According to the BJH plots (insert curves in Fig. 5), the total pore volume of CN, and ternary nanocomposite was obtained to be 0.08 cm^3 g^{-1}, and 0.148 cm^3 g^{-1}, respectively. Therefore, the as-made AgI/CN@CeO$_2$ photocatalyst has the highest surface area and pore volume, with a well-defined mesoporous structure.
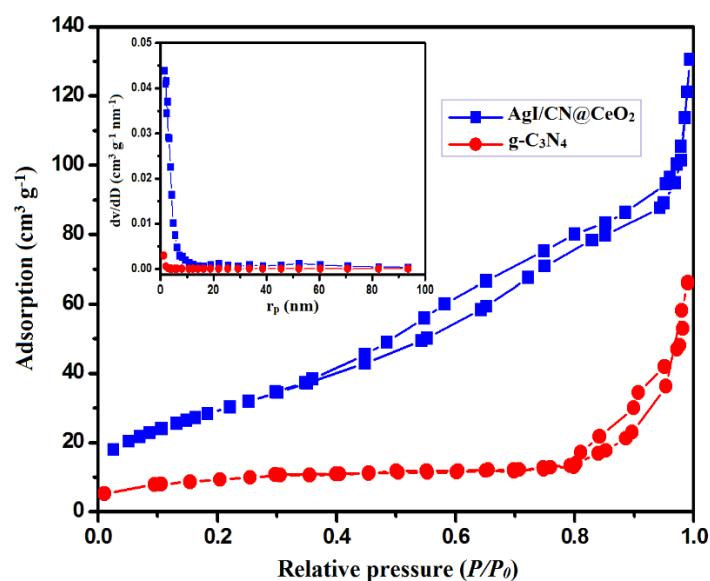
Figure 5. N$_2$ adsorption-desorption isotherms, and BJH plots of CN, and AgI/CeO$_2$@CN photocatalyst at 77 K.

3.2. Photocatalytic performance of the synthesized catalysts

3.2.1. Kinetics of the photocatalytic reduction of Cr(VI)

The catalytic performance of pure CN, CeO$_2$, AgI, CeO$_2$@CN, AgI/CeO$_2$, AgI/CN, and AgI/CeO$_2$@CN nanocomposites were investigated towards Cr(VI) reduction under visible (Vis)-light (Fig. 6a). In the

absence of catalyst, the blank testes showed that the Cr(VI) was stable, and no photodecomposition was observed under Vis light. According to obtained results, compared with CN, CeO_2, and AgI alone, the binary nanocomposite shows better photocatalytic activity in the photo-reduction of Cr(VI), due to the formation of a hetero-junction structure between two compounds. As such, the photo-catalytic reduction of Cr(VI) was efficiently promoted under visible light irradiation.

In order to obtain more information about the photocatalytic activity of as-prepared samples, the pseudo-first order (PFO) rate constant values (k_{app}) of reactions were determined by using the slope of ln (C_0/C_t) versus reaction time (t) (eq. 4), in which C_t, and C_0 are the concentration of Cr(VI) at time t, and zero, respectively.

$$\ln\left(\frac{C_0}{C_t}\right) = k_{app}t \tag{4}$$

Deposition of AgI NPs on the surface of CeO_2@CN increased the reaction rate of photo-reduction Cr(VI) under Vis light. It is worth mentioning that the highest rate constant value was obtained to be 0.058 min^{-1} for the AgI/CeO_2@CN/Vis process, which was 2.1 times higher than the calculated values for the CeO_2@CN/Vis system (0.028 min^{-1}) (Fig. 6b). These results confirmed the vital role of AgI NPs in the as-prepared nanocomposite which can promote the photocatalytic reduction of Cr(VI) solution under Vis irradiation. In addition, the photo-reduction rate over the AgI/CeO_2@CN nanocomposite is 9.7, 4.8, and 5.8 times faster than pure CN (0.006 min^{-1}), and both CeO_2 (0.012 min^{-1}) and AgI (0.01 min^{-1}), respectively.

The photocatalytic activity of the as-prepared photocatalyst was compared with other photocatalysts that were used for the reduction of Cr(VI) in literature, and the results were reported in Table 1 [53-59]. According to these results, the mass ratio (amount of catalyst per pollutant) of our photocatalyst with chromium was the smallest one in reported systems (see Table 1), and high reduction efficiency was obtained in short time. To compare the photo-activity of reported catalysts in Cr(VI) removal, the Efficacy Factor (EF) was calculated for these processes by equation 5. This factor describes the amount of the contaminants eliminated per concentration of catalyst, through

the experimental time. The calculated results are shown in Table 1. Based on the above results, our ternary AgI/CeO$_2$@CN photocatalyst showed the highest photocatalytic performance in reduction of Cr(VI) under Vis light.

$$EF = \frac{Concentration\ of\ Cr(VI)\ (mg/L)\ \times\ \%\ of\ its\ reduction}{Catalyst\ concentration\ (mg/L)\ \times\ time\ (min)} \tag{5}$$

Furthermore, for the evaluation of the efficiency of the system, two Figure of merit (FoM) parameters including electrical energy per mass (E_{E_M}), and electrical energy per order (E_{E_O}) are generally proposed for AOPs on the use of electrical energy [60]. E_{E_M} describes the amount of electrical energy (kWh) required for the removal of one kg of the pollutant from the (waste)water, while in low concentrations of pollutant (as we used here), E_{E_O} is defined as the energy needed to reduce the concentration of pollutant by one order magnitude (90%) in 1 m^3 of (waste)water (eq. 6) [61]. In this equation, P, V, and t are the power (kW) of the system, volume of reaction reactor (L), and irradiation time, respectively. E_{E_O} can be written as eq. 7 by using eqns. 4, and 6.

$$E_{E_O} = \frac{P \times t \times 1000}{V \times 60 \times \log\left(\frac{C_0}{C_t}\right)} \tag{6}$$

$$E_{E_O} = \frac{38.4 \times P}{V \times k_{app}} \tag{7}$$

According to the above equations, the E_{E_O} values for the photocatalytic processes in the presence of CN, CeO$_2$, AgI, CeO$_2$@CN, and AgI/CeO$_2$@CN were calculated to be 4200, 2297.4, 2688, 973.9, and 465.05 kWh/m^3, respectively. These results indicated the highly efficient photocatalytic performance of AgI/CeO$_2$@CN nanocomposite in photo-reduction of Cr(VI).
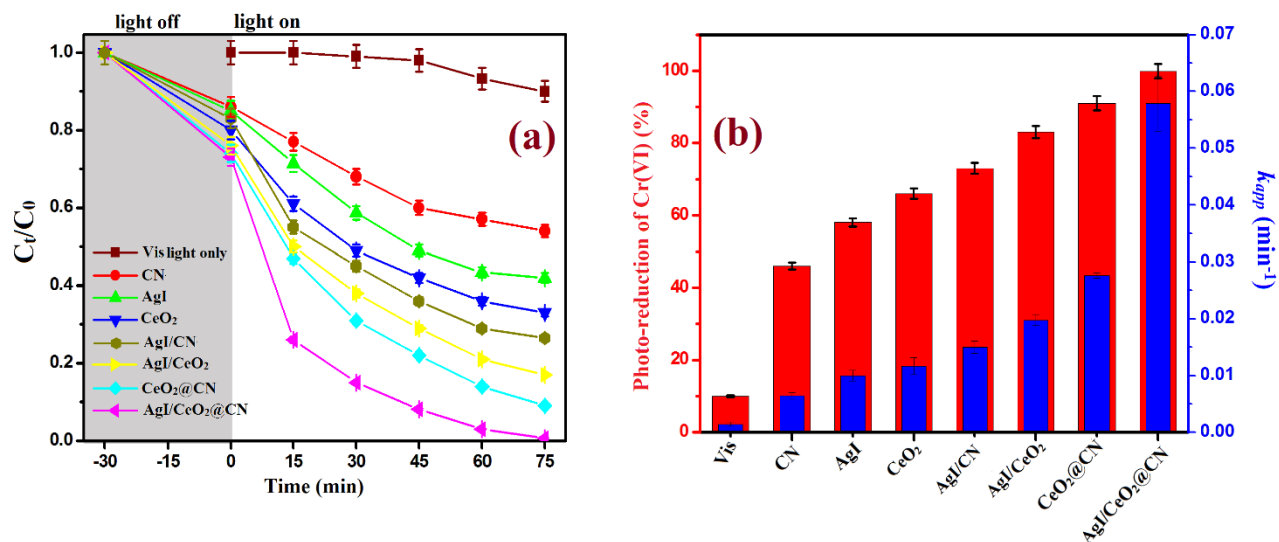
Figure 6. Photo-reduction of Cr(VI) solution over the as-prepared samples (a), and removal efficiency and PFO rate constant values of reaction (b) (Reaction conditions: [Cr(VI)] = 15 mg L^{-1}, [catalyst] = 0.2 g L^{-1}, and initial solution pH = 3.0).

Table 1. Comparison of different photocatalytic processes in reduction of Cr(VI).

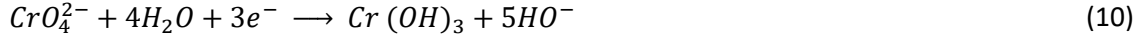| Photocatalyst	catalyst (g/L)	Cr(VI) (mg/L)	pH	Light source	Removal (%)	Time (min)	k_{app} (min^{-1})	EF	Ref.
AgI/CeO$_2$@CN	0.2	15	3.0	Vis	99.6	75	0.058	0.1	This work
PANI@g-C$_3$N$_4$/ZnFe$_2$O$_4$	1.0	20	-	Vis	75.0	120	0.011	0.001	[53]
UiO-66-NH$_2$(Zr)	0.67	5.0	2.0	Vis	98.0	120	-	0.006	[54]
ZnAlTi-LDO	0.4	5.0	5.5	LED	69.2	210	-	0.004	[16]
rGO@Cu$_2$O/BiVO$_4$	0.4	5.0	7.0	LED	88.0	240	-	0.005	[55]
CoS$_2$/g-C$_3$N$_4$-rGO	0.5	20	2.0	Vis	99.8	120	0.039	0.033	[2]
MIL(101)Fe/g-C$_3$N$_4$	0.5	20	5.0	Vis	92.6	60	-	0.062	[56]
g-C$_3$N$_4$/UiO-66	0.5	10	2.0	Xe lamp	99.0	40	0.110	0.05	[57]
AgI/BiVO$_4$	0.4	15	-	Xe lamp	70.0	100	-	0.03	[58]
AgI/BiOI-Bi$_2$O$_3$	1.0	23.5	6.08	Xe lamp	95.0	90	0.032	0.025	[59]

3.2.2. Treatment process optimization and boundary conditions

-Effect of initial solution pH value: Previous studies demonstrated that the photo-reduction of Cr(VI) to Cr(III) was influenced by the initial pH solution [58, 59]. In order to study the initial pH solution on photocatalytic reduction of Cr(VI) to Cr(III) over the AgI/CeO$_2$@CN nanocomposite, the reaction pH was varied from 2.0 to 9.0. The obtained results are illustrated in Fig. 7a. The highest photo-reduction of Cr(VI) was detected at acidic media, and by increasing the pH value, the efficiency of reaction was decreased, and lowest amount (33.0%) was obtained at pH = 9.0. Moreover, to better understand the effect of solution pH on the photo-reduction of Cr(VI) to Cr(III) at different pH values, the pseudo-first order rate constant values of the reaction were calculated form the slope of ln (C_0/C_t) versus reaction time (t). The obtained value at pH = 2.0, is 12.83, 9.64, 5.68, and 1.20 times higher than other values at pH of 9.0, 7.0, 5.0, and 3.0, respectively, which indicated the acidic media is favorable for photocatalytic reduction of Cr(VI) to Cr(III). The above results indicate that the photocatalytic reduction of Cr(VI) is greatly sensitive to pH solution which can explained by the following reasons:

- *Point of zero charge of the ternary photocatalyst*: The point of zero charge (pH$_{pzc}$) of the as-made photocatalyst is 4.6, which indicates the AgI/CeO$_2$@CN photocatalyst has a positive surface charge at pH < pH$_{pzc}$ that can enhance the adsorption of $Cr_2O_7^{2-}$ on the surface of the photocatalyst, and hence improve the reduction rate. Due to presence of an electrostatic repulsion effect at pH > 4.6, Cr(VI) had less chance to be attracted to the surface of nanocomposite and the photo-reduction efficiency was decreased. In addition, at acidic media, the dominant, and main species of chromium are $Cr_2O_7^{2-}$ anionic [3].

- *Cr speciation in the matrix*: Three kinds of ions including $Cr_2O_7^{2-}$, $HCrO_4^-$, and CrO_4^{2-} exist as dominant species at acidic, neutral, and basic conditions, respectively [61]. The photo-reduction reaction of Cr(VI) at various conditions is described by the following equations (eqns. 8-10). At low pH, due to the presence of high concentration of H$^+$ in the solution, the reduction potential increased

22

dramatically, which confirmed the photo-reduction of Cr(VI) is more favorable at acidic conditions. On the other hand, at high pH values, the active sites of nanocomposite can be covered by the Cr $(OH)_3$ that corresponding to inferior reduction efficiency (eq. 10).

$$Cr_2O_7^{2-} + 14H^+ + 6e^- \longrightarrow 2Cr^{3+} + 7H_2O \tag{8}$$

$$HCrO_4^- + 7H^+ + 3e^- \longrightarrow Cr^{3+} + 4H_2O \tag{9}$$

$$CrO_4^{2-} + 4H_2O + 3e^- \longrightarrow Cr(OH)_3 + 5HO^- \tag{10}$$

-**Effect of initial Cr(VI) concentration**: The photocatalytic efficiency of the as-made nanocomposite in the photo-reduction of Cr(VI) was investigated at various concentrations (10-100 mg/L) of Cr(VI) at initial pH solution 3.0, and 0.2 g/L of catalyst within reaction time of 75 min (Fig. 7b). The photocatalytic efficiency of the reaction was decreased from 100% to 32% when the initial concentration of Cr(VI) was increased from 10 to 100 mg/L. This behavior is related to the large amount of Cr(VI) that are adsorbed on the surface of photocatalyst and prevent the light absorption during the reaction. Consequently, under these conditions, the specific and available surface area of photocatalyst was decreased, that results to lower photocatalytic efficiency. Moreover, the PFO rate constants values at different concentrations were calculated by using eq. 4, and the results reported in Table 2. When the initial concentration of Cr(VI) was increased from 10 m/L to 100 mg/L, the PFO rate constant value was changed from 0.074 min^{-1} to 0.0046 min^{-1}. The relationship between initial concentration of Cr(VI) and reduction rate (r) can be investigated by applying the Langmuir-Hinshelwood model (eqns. 11, and 12) [61].

$$r = k_c \frac{K_{Cr(VI)} [Cr(VI)]}{1 + K_{Cr(VI)} [Cr(VI)]_0} = k_{app} [Cr(VI)] \tag{11}$$

$$\frac{1}{k_{app}} = \frac{1}{k_c K_{Cr(VI)}} + \frac{[Cr(VI)]_0}{k_c} \tag{12}$$

Where, k_c (mg/L/min), and $K_{Cr(VI)}$ (L/mg) are the kinetic rate constant of surface reaction, and the Langmuir-Hinshelwood adsorption equilibrium constants, respectively.

These values were calculated to be 0.472 mg/L/min, and 0.198 L/mg, respectively, from the slope of

$\frac{1}{k_{app}}$ versus $[Cr(VI)]_0$. The superiority of this catalyst can be demonstrated by comparison with

other works; for instance, the k_c value was reported to be 0.424 mg/L/min for removal of 20 mg/L

Cr(VI) over UV/ZnO-TiO$_2$ system [61].

In addition, the E_{E_O} values of the photocatalytic processes with different initial Cr(VI) concentrations

were calculated and summarized in Table 2. Based on the results, E_{E_O} value was increased from

363.243 to 5376 kWh/m^3 with increasing the initial Cr(VI) concentration from 10 mg/L to 100 mg/L.

Table 2. PFO kinetic parameters, and E_{E_O} of the photocatalytic reduction of Cr(VI) at different initial Cr(VI)

concentrations (Reaction conditions: [catalyst] = 0.2 g/L, and pH=3.0).

Cr(VI) (mg/L)	k_{app} (min^{-1})	$1/k_{app}$ (min)	R^2	E_{E_O} (kWh/m^3)
10	0.074	13.5	0.9971	363
15	0.058	17.5	0.9873	472
30	0.020	50.0	0.9914	1344
50	0.010	100.0	0.9853	2688
100	0.005	200.0	0.9856	5376

-Effect of photocatalyst concentration: Various doses of AgI/CeO$_2$@CN photocatalyst were used for

the photo-reduction of Cr(VI) while the initial Cr(VI) concentration and initial solution pH were

constant at 15 mg/L, and 3.0, respectively (Fig. 7c). According to the obtained results, the removal

efficiency of Cr(VI) was increased from 32% to 100% with increasing the photocatalyst concentration

from 0.04 g/L to 0.3 g/L within 60 min. In addition, the reductive kinetics of Cr(VI) were fitted to a

PFO model. Due to increasing the number of adsorption sites, and higher generation of free

electrons in the conduction band, high efficiency was obtained at higher photocatalyst

concentration [60, 62]. Although increasing the catalyst amount led to corresponding removal

increase, e.g. from 0.1 g/L to 0.2 g/L, the reaction rate was increased 3.3 times, further increase did not lead to enhancement of the performance. Therefore, 0.2 g/L was selected at optimum concentration of photocatalyst, and further experiments were performed with this concentration.
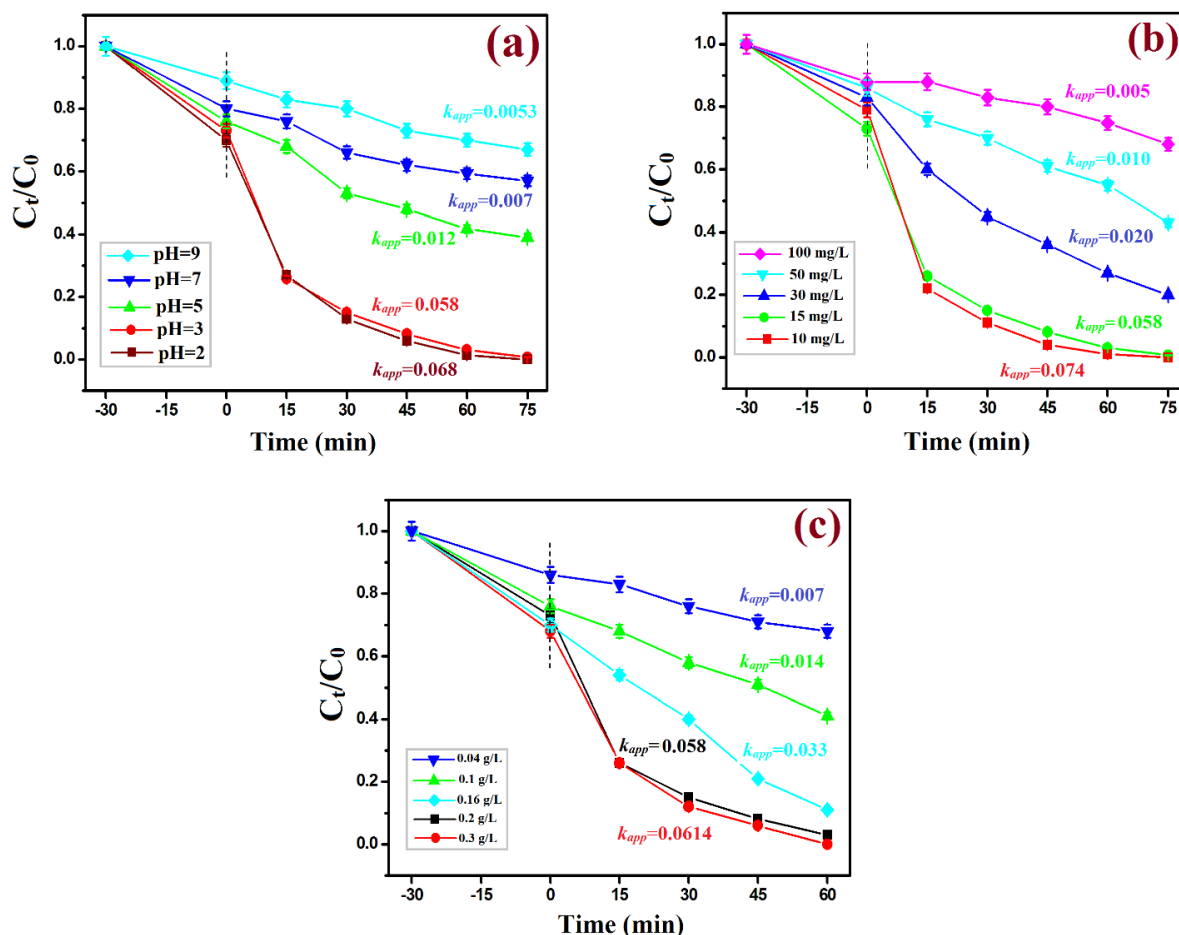

Figure 7. Effect of initial solution pH (a), Cr(VI) concentration (b), and photocatalyst dose (c) on photocatalytic reduction of Cr(VI) to Cr(III) under visible light irradiation (The dashed lines separate the adsorption (dark test) and photocatalytic reduction).

3.3. Recyclability of the synthesized ternary photocatalyst

To identify the recyclability, and chemical/structural stability of as-made nanocomposite (AgI/CeO$_2$@CN), the reaction was carried out under the same reaction conditions ([Cr(VI)] = 15 mg/L, [catalyst] = 0.2 g/L, pH = 3.0, and reaction time: 75 min) in consecutive runs at ambient temperature. The photocatalytic performance of AgI/CeO$_2$@CN nanocomposite in photocatalytic reduction of

Cr(VI) to Cr(III) only decreased about 7.2% after four repetitive cycles that confirmed the as-prepared

photocatalyst is reusable, and stable during the photocatalytic reaction (Fig. 8a). Moreover, the XRD

patterns of the pristine and reused photocatalysts are reported in Fig. 8b. All characteristic peaks

related to CN, CeO_2 and AgI NPs were observed, which confirmed the high stability of the

photocatalyst crystalline structure. The TEM image of reused photocatalyst was reported in Fig. 8c

and indicated that the morphology of catalyst was not changed notably during the photocatalytic

reactions. In addition, high structure stability was confirmed by the XPS analysis (Fig. 3). All

characteristic peaks were observed in high-resolution spectra of C1s, N1s, Ce3d, Ag3d, and I3d of

reused $AgI/CeO_2@CN$ nanocomposite.
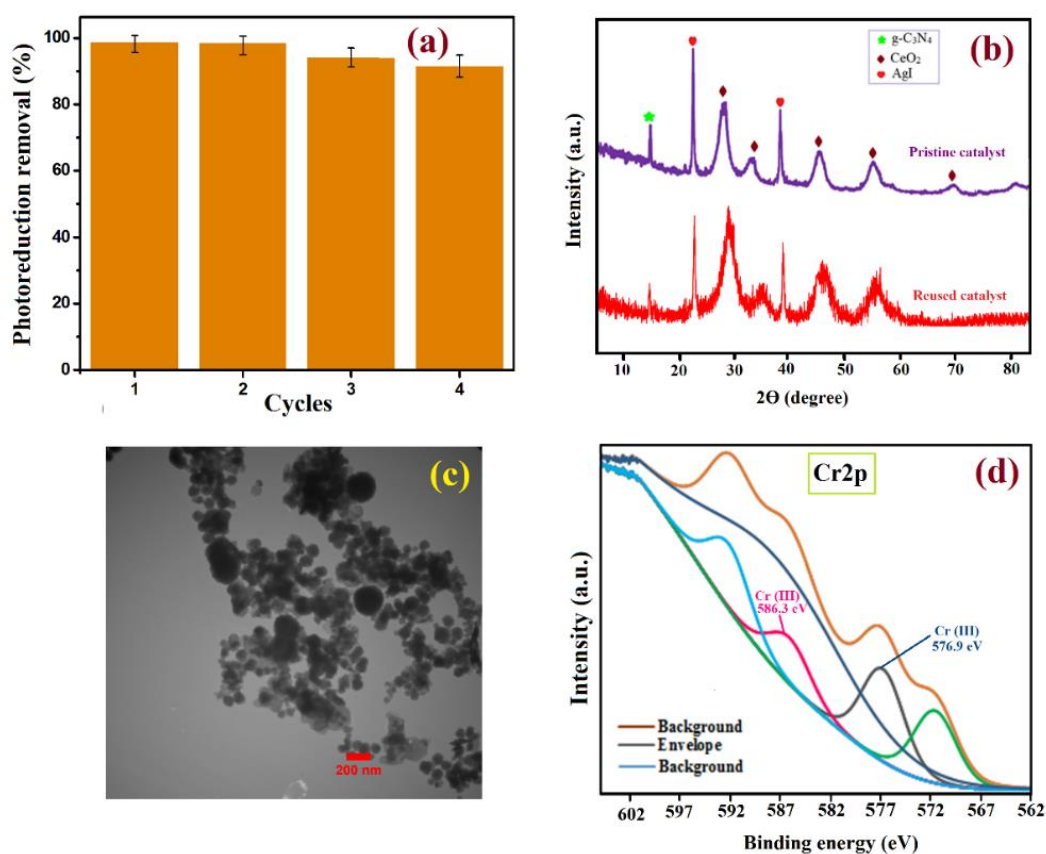
Figure 8. Photo-reduction of Cr(VI) over $AgI/CeO_2@CN$ in continuous cycles (a), XRD patterns of pristine, and

reused photocatalysts (b), TEM image of reused photocatalyst after four photocatalytic cycles (c), and high-

resolution spectra of Cr2p of re-used catalyst (d).

3.4. Reaction mechanism investigation

In order to determine the role of photo-generated reactive species during the photocatalytic reduction of Cr(VI) to Cr(III) over AgI/CeO$_2$@CN nanocomposite, radical trapping experiments were performed under optimum reaction conditions ([Cr(VI)]=15 mg/L, [catalyst]=0.2 g/L, and pH=3.0). An array of radical scavengers including p-benzoquinone (BQ), iso-propyl alcohol (IPA), potassium iodide (KI), and potassium bromate (KBrO$_3$) were applied as the scavenger of superoxide radical ($O_2^{\bullet-}$), hydroxyl radical ($HO^\bullet$), photo-generated hole (h^+), and electron (e^-), respectively [63]. The presence of IPA, and KI have low effect in the photocatalytic reduction process, hence the corresponding intermediates (h^+ and $HO^\bullet$) are not involved (Fig. 9).

By addition of BQ as $O_2^{\bullet-}$ scavenger, the reaction efficiency was decreased and reached to be 56% that confirmed the role of $O_2^{\bullet-}$ in photocatalytic reduction process. More specifically, at this pH the hydroperoxyl radical ($HO_2^\bullet$) is the dominant form (eq. 13) [63].

$$O_2^{\bullet-} + H^+ \longleftrightarrow HO_2^\bullet \quad (pK_a = 4.9) \tag{13}$$

The generation of superoxide takes place by the function of dissolved oxygen as electron acceptor. As a proof, by addition of KBrO$_3$, as an electron scavenger, the photocatalytic reduction was completely inhibited (Fig. 9). Based on the results, the photo-generated e^- and $HO_2^{\bullet-}$ were the primary reactive species in photocatalytic reduction of Cr(VI) to Cr(III) over ternary AgI/CeO$_2$@CN nanocomposite. The reaction rate constant value of photocatalytic processes in the presence of each scavenger was calculated. The lowest value of k_{app} was obtained in the presence of e^- scavenger (0.0016±4.67×10^{-5} min^{-1}). This value is 36.2 times lower than obtained value (0.058±0.0046 min^{-1}) in blank conditions, which confirmed the vital role of e^- in photocatalytic reduction of Cr(VI) in the presence of AgI/CeO$_2$@CN.

In addition, the XPS analysis after the experiment was applied to study the valence state of Cr, which was adsorbed on the surface of AgI/CeO$_2$@CN nanocomposite after the photocatalytic reduction of Cr(VI). As can be seen from the high-resolution spectra of Cr2p (Fig. 8d), the peaks at binding
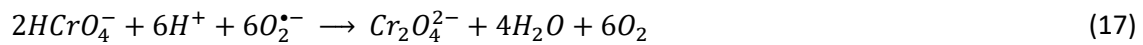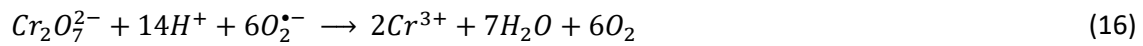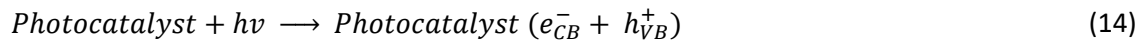
energies of 576.9 eV, and 586.3 eV corresponded to Cr2p$_{3/2}$, and Cr2p$_{1/2}$ of Cr(III), respectively [2]. This result confirmed that reduction of Cr(VI) to Cr(III) rather than plain adsorption of Cr(VI) on the photo-catalyst was the dominant Cr removal pathway surface.
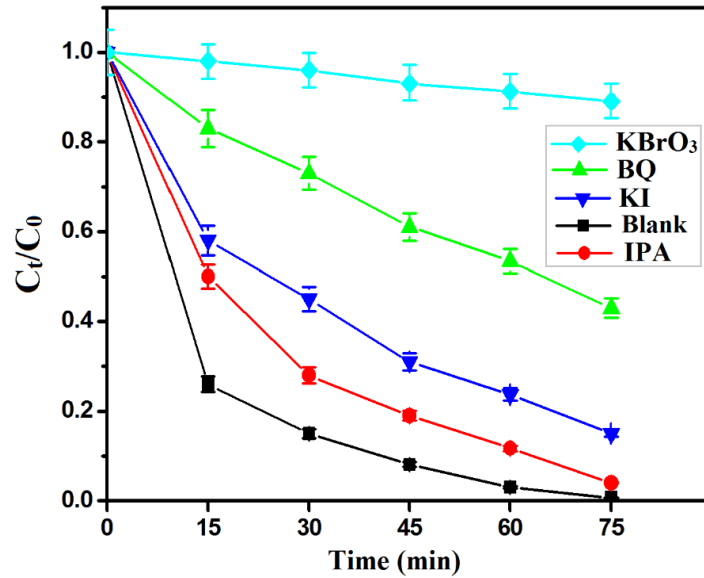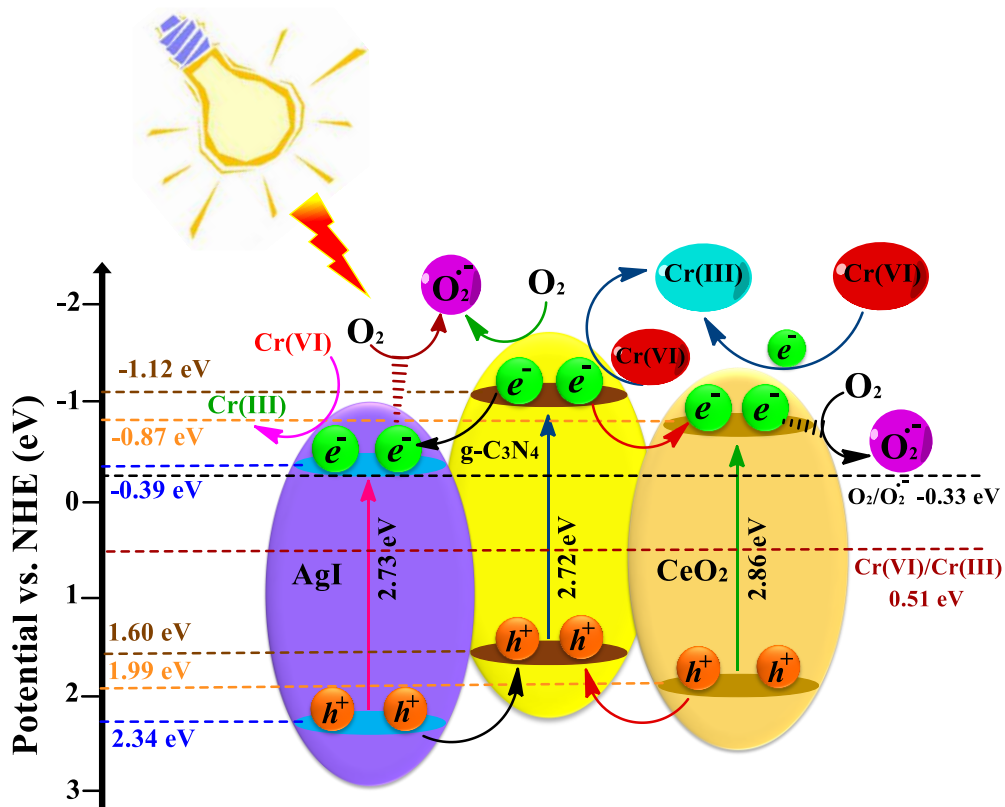

Figure 9. Scavenging effect on Cr(VI) reduction efficiency using the AgI/CeO$_2$@CN photocatalyst under visible light irradiation (Reaction conditions: ([Cr(VI)] = 15.0 mg/L, [catalyst] = 0.2 g/L, and initial pH solution = 3.0).

Based on the experimental results, a mechanism for the reduction of Cr(VI), based on the charge separation and migration over AgI/CeO$_2$@CN photocatalyst under Vis light irradiation is proposed in Fig. 10. The position of the conduction band (CB) is an important thermodynamic factor for the photo-generated electron towards its acceptor (Cr(VI)). Under light irradiation, each component, including CN, CeO$_2$ and AgI, can be excited and produce the photo-generated e^-/h^+ pairs (eq. 14). The CBs energy level of CN, CeO$_2$, and AgI are -1.12 eV, -0.87eV, and -0.39 eV, respectively. These values are more negative than the Cr(VI)/Cr(III) potential (+0.51 eV *vs*. NHE) [64], which indicated the reduction of adsorbed Cr(VI) to Cr(III) is thermodynamically favorable on CB of photocatalyst during the reaction. The CB potential of CN is more negative than those of CeO$_2$ and AgI, indicating that the photo-generated e^- can be transferred to the CB of CeO$_2$, and AgI. On the other hand, since the VB edges of AgI (+2.34 eV *vs*. NHE) and CeO$_2$ (+1.99 eV *vs*. NHE) were both more positive than

28

the VB of CN (+1.60 eV *vs*. NHE), the photo-generated holes in VB edges of AgI, and CeO_2 can be transferred to VB edge of CN. The photo-generated e^- in CB of semiconductors can participate in the photocatalytic reduction of Cr(VI) to Cr(III) as a main reactive species. Consequently, the CB potentials of CN, CeO_2, and AgI are more negative than potential of $O_2/O_2^{\bullet-}$ (-0.33 eV) [28]. Hence, over the nanocomposite the oxygen molecules can easily convert to $O_2^{\bullet-}$, and react with Cr(VI) resulting formation of Cr(III) (eqns. 15-17). In the acidic media, $Cr_2O_7^{2-}$, and $HCrO_4^-$ can react with $O_2^{\bullet-}$ resulting in the formation of Cr^{3+} and $Cr_2O_4^{2-}$, respectively [65]. Based on the scavenger experiments (Fig. 9), a non-radical pathway [66], i.e. the photo-generated e^-, has the most critical role in photocatalytic reduction of Cr(VI) to Cr(III) over AgI/CeO_2@CN catalyst (eq. 18).

$$Photocatalyst + hv \longrightarrow Photocatalyst\ (e_{CB}^- + h_{VB}^+) \qquad (14)$$

$$e_{CB}^- + O_2 \longrightarrow O_2^{\bullet-} \qquad (15)$$

$$Cr_2O_7^{2-} + 14H^+ + 6O_2^{\bullet-} \longrightarrow 2Cr^{3+} + 7H_2O + 6O_2 \qquad (16)$$

$$2HCrO_4^- + 6H^+ + 6O_2^{\bullet-} \longrightarrow Cr_2O_4^{2-} + 4H_2O + 6O_2 \qquad (17)$$

$$Cr^{6+} + e_{CB}^- \longrightarrow 2Cr^{3+} \qquad (18)$$

Figure 10. Proposed mechanism of the photocatalytic reduction of Cr(VI) over the AgI/CeO₂@CN nanocomposite.

4. Conclusions

A ternary AgI/CeO$_2$@CN photocatalyst, for the effective reduction of Cr(VI) under visible light, was successfully fabricated and characterized. The combination of AgI with CeO$_2$@CN catalyst could significantly enhance the photocatalytic efficiency of Cr(VI) reduction. The as-made photocatalyst showed the best performance at acidic conditions, achieving high removal of Cr(VI) (more than 99% in 75 min), and more than 91% removal efficiency after four catalytic cycles under the optimum reaction conditions. The excellent photocatalytic performance can be related to the efficient separation of photo-generated electron/holes (e^-/h^+) pairs through the ternary AgI/CeO$_2$@CN nanocomposite. Moreover, the E_{E_O} value for photocatalytic reduction of Cr(VI) was lower in AgI/CeO$_2$@CN/Vis process than in CeO$_2$@CN/Vis, CeO$_2$/Vis, and CN/Vis processes, which confirmed the better performance of ternary nanocomposite in this reaction due to enhanced charge separation. Based on Langmuir-Hinshelwood (L-H) model, the values of kinetic rate of surface reaction, and L-H adsorption constants were obtained as 0.472 mg/L/min, and 0.198 L/mg, respectively. The proposed photocatalytic mechanism was also supported by scavenger experiments that indicated the vital role of photo-generated e^-, and $O_2^{\bullet-}$ in photo-reduction of Cr(VI). As such, this nanocomposite can be used as promising candidate for Cr removal in further applications, e.g. in drinking water Cr remediation.

5. Acknowledgments

References

[1] J. Pradhan, S. N. Das, R. S. Thakur, Adsorption of hexavalent chromium from aqueous solution by using activated red mud. *J. Colloid. Interface. Sci*., 217 (1999) 137-141. https://doi.org/10.1006/jcis.1999.6288.

[2] Y. Wang, S. Bao, Y. Liu, W. Yang, Y. Yu, M. Feng, K. Li, Efficient photocatalytic reduction of Cr(VI) in aqueous solution over CoS_2/g-C_3N_4-rGO nanocomposites under visible light. *Appl. Surf. Sci*., 510 (2020) 145495. https://doi.org/10.1016/j.apsusc.2020.145495.

[3] G. Moussavi, F. Jiani, S. Shekoohiyan, Advanced reduction of Cr(VI) in real chrome-plating wastewater using a VUV photoreactor: batch and continuous-flow experiments. *Sep. Purif. Technol.*, 151 (2015) 218-224. https://doi.org/10.1016/j.seppur.2015.07.047.

[4] Chromium in Drinking-water Background document for development of WHO Guidelines for drinking-water quality, 2nd ed., vol. 2. Health criteria and other supporting information. World Health Organization, Geneva, 1996.

[5] X. Wang, Y.H. Liang, W.J. An, J.S. Hu, Y.F. Zhu, W.Q. Cui, Removal of chromium (VI) by a self-regenerating and metal free g-C_3N_4/graphene hydrogel system via the synergy of adsorption and photo-catalysis under visible light. *Appl. Catal. B: Environ*. 219 (2017) 53-62. https://doi.org/10.1016/j.apcatb.2017.07.008.

[6] B. Nanda, A. C. Pradhan, K. M. Parida, Fabrication of mesoporous CuO/ZrO_2-MCM-41 nanocomposites for photocatalytic reduction of Cr(VI). *Chem. Eng. J.*, 316 (2017) 1122-1135. https://doi.org/10.1016/j.cej.2016.11.080.

[7] Y. Wang, L. Yu, R. Wang, Y. Wang, X. Zhang, A novel cellulose hydrogel coating with nanoscale Fe^0 for Cr(VI) adsorption and reduction. *Sci. Total. Environ*, 726 (2020) 138625. https://doi.org/10.1016/j.scitotenv.2020.138625.

[8] R. Zhao, X. Li, B. Sun, Y. Li, Y. Li, R. Yang, C. Wang, Branched polyethylenimine grafted electrospun polyacrylonitrile fiber membrane: a novel and effective adsorbent for Cr(VI) remediation in wastewater. *J. Mater. Chem. A*, 5 (2017) 1133-1144. https://doi.org/10.1039/C6TA09784G.

[9] F. Yao, M. Jia, Q. Yang, K. Luo, F. Chen, Y. Zhong, L. He, Z. Pi, K. Hou, D. Wang, X. Li, Electrochemical Cr(VI) removal from aqueous media using titanium as anode: Simultaneous indirect electrochemical reduction of Cr(VI) and in-situ precipitation of Cr(III). *Chemosphere*, 260 (2020) 127537. https://doi.org/10.1016/j.chemosphere.2020.127537.

[10] Z. Ye, X. Yin, L. Chen, X. He, Z. Lin, C. Liu, S. Ning, X. Wang, Y. Wei, An integrated process for removal and recovery of Cr(VI) from electroplating wastewater by ion exchange and reduction-precipitation based on a silica-supported pyridine resin. *J. Clean. Prod*. 236 (2019) 117631. https://doi.org/10.1016/j.jclepro.2019.117631.

[11] B. Xie, C. Shan, Z. Xu, X. Li, X. Zhang, J. Chen, B. Pan, One-step removal of Cr(VI) at alkaline pH by UV/sulfite process: reduction to Cr(III) and in situ Cr(III) precipitation, *Chem. Eng. J*. 308 (2016) 791-797. https://doi.org/10.1016/j.cej.2016.09.123.

[12] X. Wei, Z. Gan, Y. Shen, Z. Qiu, L. Fang, B. Zhu, Negatively-charged nanofiltration membrane and its hexavalent chromium removal performance, *J. Colloid Interface Sci*. 553 (2019) 475-483, https://doi.org/10.1016/j.jcis.2019.06.051.

[13] J. Chen, X. Zhang, X. Shi, F. Bi, Y. Yang, Y. Wang, Synergistic effects of octahedral TiO_2-MIL-101(Cr) with two heterojunctions for enhancing visible-light photocatalytic degradation of liquid tetracycline and gaseous toluene. *J. Colloid. Inter. Sci*., 579 (2020) 37-49. https://doi.org/10.1016/j.jcis.2020.06.042.

[14] Y. Yang, Z.Zheng, M. Yang, J. Chen, C. Li, C. Zhang, X. Zhang, In-situ fabrication of a spherical-shaped Zn-Al hydrotalcite with BiOCl and study on its enhanced photocatalytic mechanism for perfluorooctanoic acid removal performed with a response surface methodology. *J. Hazard. Mater*, 399 (2020) 123070. https://doi.org/10.1016/j.jhazmat.2020.123070.

[15] X. Zhang, J. Chen, S. Jiang, X. Zhang, F. Bi, Y. Yang, Y. Wang, Z. Wang, Enhanced photocatalytic degradation of gaseous toluene and liquidus tetracycline by anatase/rutile titanium dioxide with heterophase junction derived from materials of Institut Lavoisier-125(Ti): Degradation pathway and mechanism studies. *J. Colloid Interface. Sci*., 588 (2021) 122-137. https://doi.org/10.1016/j.jcis.2020.12.042.

[16] J. Ye, J. Liu, Z. Huang, S. Wu, X. Dai, L. Zhang, L. Cui, Effect of reduced graphene oxide doping on photocatalytic reduction of Cr(VI) and photocatalytic oxidation of tetracycline by ZnAlTi layered double oxides under visible light. *Chemosphere* 227 (2019) 505-513. https://doi.org/10.1016/j.chemosphere.2019.04.086.

[17] S. Rengaraj, S. Venkataraj, J. W. Yeon, Y. Kim, X. Z. Li, G. K. H. Pang, Preparation, characterization and application of Nd-TiO_2 photocatalyst for the reduction of Cr(VI) under UV light illumination. *Appl. Catal. B: Environ*, 77 (2007) 157-165. https://doi.org/10.1016/j.apcatb.2007.07.016.

[18] L. Wang, N. Wang, L. Zhu, H. Yu, H. Tang, Photocatalytic reduction of Cr(VI) over different TiO_2 photocatalysts and the effects of dissolved organic species. *J. Hazard. Mater*, 152 (2008) 93-99. https://doi.org/10.1016/j.jhazmat.2007.06.063.

[19] Y. Deng, L. Tang, G. Zeng, Z. Zhu, M. Yan, Y. Zhou, J. Wang, Y. Liu, J. Wang, Insight into highly efficient simultaneous photocatalytic removal of Cr(VI) and 2,4-diclorophenol under visible light irradiation by phosphorus doped porous ultrathin g-C_3N_4 nanosheets from aqueous media: performance and reaction mechanism. *Appl. Catal. B: Environ*, 203 (2017) 343-354. https://doi.org/10.1016/j.apcatb.2016.10.046.

[20] S. H. Ri, F. Bi, A. Guan, X. Zhang, Manganese-cerium composite oxide pyrolyzed from metal organic framework supporting palladium nanoparticles for efficient toluene oxidation. *J. Colloid Interface. Sci.*, 586 (2021) 836-846. https://doi.org/10.1016/j.jcis.2020.11.008.

[21] S. Chen, Y. Hu, S. Meng, X. Fu, Study on the separation mechanisms of photogenerated electrons and holes for composite photocatalysts g-C_3N_4-WO_3. *Appl. Catal. B: Environ*, 150-151 (2014) 564-573. https://doi.org/10.1016/j.apcatb.2013.12.053.

[22] Y. He, J. Cai, L. Zhang, X. Wang, H. Lin, B. Teng, L. Zhao, W. Weng, H. Wan, M. Fan, Comparing two new composite photocatalysts, t-$LaVO_4$/g-C_3N_4 and m-$LaVO_4$/g-C_3N_4, for their structures and performances, *Ind. Eng. Chem. Res.*, 53 (2014) 5905-5915. https://doi.org/10.1021/ie4043856.

[23] M. Kohantorabi, M. R. Gholami, Fabrication of novel ternary Au/CeO_2@g-C_3N_4 nanocomposite: kinetics and mechanism investigation of 4-nitrophenol reduction, and benzyl alcohol oxidation. *Appl. Phys. A.*, 124 (2018) 441. https://doi.org/10.1007/s00339-018-1858-0.

[24] J. Luo, X. Zhou, L. Ma, X. Xu, Enhancing visible-light photocatalytic activity of g-C_3N_4 by doping phosphorus and coupling with CeO_2 for the degradation of methyl orange under visible light irradiation. *RSC Adv.*, 5 (2015) 68728-68735. https://doi.org/10.1039/C5RA10848A.

[25] W.X. Zou, B. Deng, X.X. Hu, Y.P. Zhou, Y. Pu, S.H. Yu, K.L. Ma, J.F. Sun, H.Q. Wan, L. Dong, Crystal-plane-dependent metal oxide-support interaction in CeO_2/g-C_3N_4 for photocatalytic hydrogen evolution, *Appl, Catal. B.* 238 (2018) 111-118. https://doi.org/10.1016/j.apcatb.2018.07.022.

[26] H. B. Song, R. Y. Wu, J. F. Yang, J. C. Dong, G. J. Ji, Fabrication of CeO_2 nanoparticles decorated three-dimensional flower-like BiOI composites to build p-n heterojunction with highly enhanced visible-light photocatalytic performance, *J. Colloid Interface Sci.* 512 (2018) 325-334. https://doi.org/10.1016/j.jcis.2017.10.080.

[27] X. Zhao, P. Wu, Y. Lei, F. Chen, Z. Yu, P. Fang, Y. Liu, Sun-light-driven plasmonic Ag/AgCl@TNT photocatalysts for high-efficient absorption-regeneration and photocatalytic degradation. *Appl. Surf. Sci.*, 529 (2020) 147010. https://doi.org/10.1016/j.apsusc.2020.147010.

[28] H. Salari, M. Kohantorabi, Facile template-free synthesis of new a-MnO$_2$ nanorod/silver iodide p-n junction nanocomposites with high photocatalytic performance. *New J. Chem*. 44 (2020) 7401-7411. https://doi.org/10.1039/D0NJ01033B.

[29] X. J. Wen, C. H. Shen, Z. H. Fei, D. Fang, Z. T. Liu, J. T. Dai, C. G. Niu, Recent developments on AgI based heterojunction photocatalytic systems in photocatalytic application. *Chem. Eng. J.,* 383 (2020) 123083. https://doi.org/10.1016/j.cej.2019.123083.

[30] L. Zhou, W. Zhang, L. Chen, H. Deng, J. Wan, A novel ternary visible-light-driven photocatalyst AgCl/Ag$_3$PO$_4$/g-C$_3$N$_4$: synthesis, characterization, photocatalytic activity for antibiotic degradation and mechanism analysis. *Catal. Commun*, 100 (2017) 191-195. https://doi.org/10.1016/j.catcom.2017.06.049.

[31] M. Tang, Y. Ao, C. Wang, P. Wang, Facile synthesis of dual Z-scheme g-C$_3$N$_4$/Ag$_3$PO$_4$/AgI composite photocatalysts with enhanced performance for the degradation of a typical neonicotinoid pesticide. *Appl. Catal. B: Environ,* 268 (2020) 118395. https://doi.org/10.1016/j.apcatb.2019.118395.

[32] J. Zhang, Z. Zhu, J. Jiang, H. Li, Fabrication of a novel AgI/LaFeO$_3$/g-C$_3$N$_4$ dual Z-scheme photocatalyst with enhanced photocatalytic performance. *Mater. Letter*, 262 (2020) 127029. https://doi.org/10.1016/j.matlet.2019.127029.

[33] Y. Yuan, G. F. Huang, W. Y. Hu, D. N. Xiang, B. X. Zhou, S. Chang, W. Q. Huang, Construction of g-C$_3$N$_4$/CeO$_2$/ZnO ternary photocatalysts with enhanced photocatalytic performance. *J. Phys. Chem. Solid*, 106 (2017) 1-9. https://doi.org/10.1016/j.jpcs.2017.02.015.

[34] J. Rashid, A. Abbas, L. C. Chang, A. Iqbal, I. U. Haq, A. Rehman, S. U. Awan, M. Rafique, M. A. Barakat, Butterfly cluster like lamellar BiOBr/TiO$_2$ nanocomposite for enhanced sunlight photocatalytic mineralization of aqueous ciprofloxacin. *Sci. Total. Environ*, 665 (2019) 668-677. https://doi.org/10.1016/j.scitotenv.2019.02.145.

[35] M. Li, C. Song, Y. Wu, M. Wang, Z. Pan, Y. Sun, L. Meng, S. Han, L. Xu, L. Gan, Novel Z-scheme visible-light photocatalyst based on $CoFe_2O_4/BiOBr/Graphene$ composites for organic dye degradation and Cr(VI) reduction. *Appl. Surf. Sci.*, 478 (2019) 744-753. https://doi.org/10.1016/j.apsusc.2019.02.017.

[36] F. Chen, C. Yu, L. Wei, Q. Fan, F. Ma, J. Zeng, J. Yi, K. Yang, H. Ji, Fabrication and characterization of $ZnTiO_3/Zn_2Ti_3O_8/ZnO$ ternary photocatalyst for synergetic removal of aqueous organic pollutants and $Cr(_{VI})$ ions. *Sci. Total. Environ*, 706 (2020) 136026. https://doi.org/10.1016/j.scitotenv.2019.136026.

[37] APHA, AWWA, WPCF, Standard Methods for the Examination of Water and Wastewater, 21st ed., Public Health Association, Washington DC, 2005.

[38] Ansari, A.A., P.R. Solanki and B.D. Malhotra, Hydrogen peroxide sensor based on horse radish peroxidase immobilized nanostructured cerium oxide film. *J. Biotechnol*., 142 (2009) 179-184. https://doi.org/10.1016/j.jbiotec.2009.04.005.

[39] B. Zhu, P. Xia, Y. Li, W. Ho, J. Yu, Fabrication and photocatalytic activity enhanced mechanism of direct Z-scheme $g-C_3N_4/Ag_2WO_4$ photocatalyst. *Appl. Surf. Sci.*, 391 (2017) 175-183. https://doi.org/10.1016/j.apsusc.2016.07.104.

[40] F. Fazlali, A. Hajian, A. Afkhami, H. Bagheri, A superficial approach for fabricating unique ternary $AgI@TiO_2/Zr-MOF$ composites: An excellent interfacial with improved photocatalytic light-responsive under visible light. *J. Photochem. Photobiol. A.*, 400 (2020) 112717. https://10.1016/j.jphotochem.2020.112717.

[41] X.G. Zhang, D.L. Guan, C.G. Niu, Z. Cao, C. Liang, N. Tang, L. Zhang, X.J. Wen, G.M. Zeng, Constructing magnetic and high-efficiency $AgI/CuFe_2O_4$ photocatalysts for inactivation of *Escherichia coli* and *Staphylococcus aureus* under visible light: inactivation performance and mechanism analysis. *Sci. Total. Environ*, 668 (2019) 730-742. https://doi.org/10.1016/j.scitotenv.2019.03.068.

[42] X. Zhang, Y. Yang, W. Huang, Y. Yang, Y. Wang, C. He, N. Liu, M. Wu, L. Tang, g-C_3N_4/UiO-66 nanohybrids with enhanced photocatalytic activities for the oxidation of dye under visible light irradiation. *Mater. Res. Bull*., 99 (2018) 349-358. https://doi.org/10.1016/j.materresbull.2017.11.028.

[43] H. Xu, T. Zhang, Y. Gu, X. Yan, N. Lu, H. Liu, Z. Xu, Y. Xing, Y. Song, Z. Zhang, M. Yang, An electrochemical thrombin aptasensor based on the use of graphite-like C_3N_4 modified with silver nanoparticles. *Microchimica Acta*, 187 (2020) 163. https://doi.org/10.1007/s00604-020-4111-4.

[44] X. Zhang, F. Hou, Y. Yang, Y. Wang, N. Liu, D. Chen, Y. Yang, A facile synthesis for cauliflower like CeO_2 catalysts from Ce-BTC precursor and their catalytic performance for CO oxidation. *Appl. Surf. Sci*., 423 (2017) 771-779. http://dx.doi.org/doi:10.1016/j.apsusc.2017.06.235.

[45] R. E. Adam, E. Chalangar, M. Pirhashemi, G. Pozina, X. Liu, J. Palisaitis, H. Pettersson, M. Willander, O. Nur, Graphene-based plasmonic nanocomposite for highly enhanced solar-driven photocatalytic activities. *RSC Adv*., 9 (2019) 30585. https://doi.org/10.1039/C9RA06273D.

[46] X. Zhang, L. Song, F. Bi, D. Zhang, Y. Wang, L. Cui, Catalytic oxidation of toluene using a facile synthesized Ag nanoparticle supported on UiO-66 derivative. *J. Colloid Interface. Sci*., 571 (2020) 38-47. https://doi.org/10.1016/j.jcis.2020.03.031.

[47] H. Salari, M. Kohantorabi, Fabrication of novel Fe_2O_3/MoO_3/AgBr nanocomposites with enhanced photocatalytic activity under visible light irradiation for organic pollutant degradation. *Adv. Powder. Technol*, 31 (2020) 493-503. https://doi.org/10.1016/j.apt.2019.11.005.

[48] M. Kohantorabi, S. Giannakis, G. Moussavi, B. Bensimon, M. R. Gholami, C. Pulgarin, An innovative, highly stable Ag/ZIF-67@GO nanocomposite with exceptional peroxymonosulfate (PMS) activation efficacy, for the destruction of chemical and microbiological contaminants under visible light. *J. Hazard. Mater*, 413 (2021) 125308. https://doi.org/10.1016/j.jhazmat.2021.125308.

[49] A.H.C. Khavar, G. Moussavi, A. Mahjoub, K. Yaghmaeian, V. Srivastava, M. Sillanpaa, M. Satari, Novel magnetic Fe_3O_4@rGO@ZnO onion-like microspheres decorated with Ag nanoparticles for the efficient photocatalytic oxidation of metformin: toxicity evaluation and insights into the mechanisms. *Catal. Sci. Technol*., 9 (2019) 5819-5837. https://doi.org/10.1039/C9CY01381D.

[50] A. Rehman, Y. J. Heo, G. Nazir, Solvent-free, one-pot synthesis of nitrogen-tailored alkali-activated microporous carbons with an efficient CO_2 adsorption. *Carbon*, 172 (2021) 71-82. https://doi.org/10.1016/j.carbon.2020.09.088.

[51] X. Shi, X. Zhang, F. Bi, Z. Zheng, L. Sheng, J. Xu, Z. Wang, Y. Yang, Effective toluene adsorption over defective UiO-66-NH_2: An experimental and computational exploration. *J. Mol. Liq*., 316 (2020) 113812. https://doi.org/10.1016/j.molliq.2020.113812.

[52] G. Nazir, A. Rehman, S. J. Park, Sustainable N-doped hierarchical porous carbons as efficient CO_2 adsorbents and high-performance supercapacitor electrodes. *J. CO_2. Utilize*, 42 (2020) 101326. https://doi.org/10.1016/j.jcou.2020.101326.

[53] S. Patnaik, K. K. Das, A. Mohanty, K. Parida, Enhanced photo catalytic reduction of Cr(VI) over polymer-sensitized g-C_3N_4/$ZnFe_2O_4$ and its synergism with phenol oxidation under visible light irradiation. *Catal. Today*, 315 (2018) 52-66. https://doi.org/10.1016/j.cattod.2018.04.008.

[54] X. D. Du, X. H. Yi, P. Wang, W. Zheng, J. Deng, C. C. Wang, Robust photocatalytic reduction of Cr(VI) on UiO-66-NH_2(Zr/Hf) metal-organic framework membrane under sunlight irradiation. *Chem. Eng. J*., 356 (2019) 393-399. https://doi.org/10.1016/j.cej.2018.09.084.

[55] Z. Huang, X. Dai, Z. Huang, T. Wang, L. Cui, J. Ye, P. Wu, Simultaneous and efficient photocatalytic reduction of Cr(VI) and oxidation of trace sulfamethoxazole under LED light by rGO@Cu_2O/$BiVO_4$ p-n heterojunction composite. *Chemosphere* 221 (2019) 824-833. https://doi.org/10.1016/j.chemosphere.2019.01.087.

[56] F. Zhao, Y. Liu, S. B. Hammouda, B. Doshi, N. Guijarro, X. Min, C. J. Tang, M. Sillanpao, K. Sivula, S. Wang, MIL-101(Fe)/g-C_3N_4 for enhanced visible-light-driven photocatalysis toward

simultaneous reduction of Cr(VI) and oxidation of bisphenol A in aqueous media. *Appl. Catal. B: Environ*, 272 (2020) 119033. https://doi.org/10.1016/j.apcatb.2020.119033.

[57] X. H. Yi, S. Q. Ma, X. D. Du, C. Zhao, H. Fu, P. Wang, C. C. Wang, The facile fabrication of 2D/3D Z-scheme g-C$_3$N$_4$/UiO-66 heterojunction with enhanced photocatalytic Cr(VI) reduction performance under white light. *Chem. Eng. J.*, 375 (2019) 121944. https://doi.org/10.1016/j.cej.2019.121944.

[58] W. Zhao, J. Li, B. Dai, Z. Cheng, J. Xu, K. Ma, L. Zhang, N. Sheng, G. Mao, H. Wu, K. Wei, D. Y. C. Leung, Simultaneous removal of tetracycline and Cr(VI) by a novel three-dimensional AgI/BiVO$_4$ p-n junction photocatalyst and insight into the photocatalytic mechanism. *Chem. Eng. J.*, 369 (2019) 716-725. https://doi.org/10.1016/j.cej.2019.03.115.

[59] Q. Wang, X. Shi, E. Liu, J. C. Crittenden, X. Ma, Y. Zhang, Y. Cong, Facile synthesis of AgI/BiOI-Bi$_2$O$_3$ multi-heterojunctions with high visible light activity for Cr(VI) reduction. *J. Hazard. Mater*, 317 (2016) 8-16. https://doi.org/10.1016/j.jhazmat.2016.05.044.

[60] G.C. Yang, S.W. Chan, Photocatalytic reduction of chromium(VI) in aqueous solution using dye-sensitized nanoscale ZnO under visible light irradiation. *J. Nanopart. Res*. 11 (2009) 221. https://doi.org/10.1007/s11051-008-9423-y.

[61] M. Naimi-Joubani, M. Shirzad-Sibani, J. K. Yang, M. Gholami, M. Farzadkia, Photocatalytic reduction of hexavalent chromium with illuminated ZnO/TiO$_2$ composite. *J. Indust. Eng. Chem.*, 22 (2015) 317-323. https://doi.org/10.1016/j.jiec.2014.07.025.

[62] B. Xie, H. Zhang, P. Cai, R. Qiu, Y. Xiong, Simultaneous photocatalytic reduction of Cr(VI) and oxidation of phenol over monoclinic BiVO$_4$ under visible light irradiation. *Chemosphere,* 63 (2006) 956-963. https://doi.org/10.1016/j.chemosphere.2005.08.064.

[63] S. Shekoohiyan, A. Rahmania, M. Chamak, G. Moussavi, O. Rahmanian, V. Alipour, S. Giannakis, A novel CuO/Fe$_2$O$_3$/ZnO composite for visible-light assisted photocatalytic oxidation of Bisphenol

A: kinetics, degradation pathways, and toxicity elimination. *Sep. Purif. Technol*., 242 (2020) 116821. https://doi.org/10.1016/j.seppur.2020.116821.

[64] D. Hao, Q. Shen, J. Liu, L. Wei, R. Bibi, B. Fu, N. Li, J. Zhou, Integration of CdS particles into sodium alginate aerogel with enhanced photocatalytic performance. *Inter. J. Biol. Macro*, 141 (2019) 1111-1117. https://doi.org/10.1016/j.ijbiomac.2019.09.064.

[65] F. Wang, X. Liu, L. Xu, X. Zheng, One-pot synthesis of CeO_2/Mg-Al layered double oxide nanosheets for efficient visible-light induced photo-reduction of Cr(VI). *Colloid. Surf. A.*, 601 (2020) 125044. https://doi.org/10.1016/j.colsurfa.2020.125044.

[66] M. Kohantorabi, G. Moussavi, S. Giannakis, A review of the innovation in metal-and carbon-based catalysts explored for heterogeneous peroxymonosulfate (PMS) activation, with focus on radical *vs*. non-radical degradation pathways of organic contaminants. *Chem. Eng. J*., 411 (2021) 127957. https://doi.org/10.1016/j.cej.2020.127957.